Exploring the Feasibility of Ion Beam Gyroscope Based on Corona Discharge

by

Liu Xuehan

B.Sc., Sichuan University, 2014

Thesis Submitted in Partial Fulfillment of the
Requirements for the Degree of
Master of Applied Science

in the
School of Engineering Science
Faculty of Applied Science

© Liu Xuehan 2017
SIMON FRASER UNIVERSITY
Fall 2017

All rights reserved.
However, in accordance with the *Copyright Act of Canada*, this work may be reproduced without authorization under the conditions for "Fair Dealing."
Therefore, limited reproduction of this work for the purposes of private study, research, education, satire, parody, criticism, review and news reporting is likely to be in accordance with the law, particularly if cited appropriately.

Approval

Name:	**Liu Xuehan**
Degree:	**Master of Applied Science (Engineering Science)**
Title:	***Exploring the Feasibility of Ion Beam Gyroscope Based on Corona Discharge***
Examining Committee:	**Chair:** Steve Whitmore Senior Lecturer

Albert Leung
Senior Supervisor
Professor Emeritus

John Jones
Supervisor
Professor Emeritus

Ash Parameswaran
Supervisor
Professor

Behraad Bahreyni
Internal Examiner
Associate Professor
Department of Mechatronic Systems Engineering

Date Defended: 1 September 2017

Abstract

An ion beam gyroscope has been proposed to measure the speed of rotating, which is potentially inexpensive and free of the mechanical stress. The characteristics of the low-pressure corona gas discharge in a compact discharge tube are studied to obtain a sufficient and stable ion beam source for ion beam gyroscopes. Ions moving to the cathode by the effect of an electric field can produce a current signal. If a dual-cathode discharge device is used, currents going to the two cathodes are denoted by I_1 and I_2 respectively. If the device is placed on a rotating platform, ions will be deflected by the Coriolis effect. Thus, I_1 and I_2 change accordingly with rotating speeds. Consequently, the differential current between the variation of each cathode is a function of the Coriolis acceleration rate. Since a magnetic field can deflect ions in the same way as the Coriolis effect, a magnetic field is used to simulate the Coriolis effect to avoid the rotating platform in the early exploring stage. This replacement allows us to have a simpler experimental setup, and the magnetic field is also easier to control.

A theoretical model has been derived to describe the motion of ions in the discharge tube. Emulation experiments were conducted to explore the correlation between speed of rotating and differential current, relevant variables and their impacts on the sensitivity of ion beam gyroscopes. These experiments demonstrate the ion beam gyroscope is feasible, although the device's sensitivity is limited by 1.6 pA/rpm.

Keywords: Corona Discharge; Ion Beam Gyroscope; Ion Deflection

Acknowledgements

I would like to express my deepest gratitude to my senior supervisor, Dr. Albert Leung. Thanks for his endless help, great patience and insightful criticism of my project in my Master's career. His wisdom and enthusiasm in research have been significantly influenced and motivated me in my life. It is very rewarding and honored to work with him.

My appreciation also goes to my supervisor, Dr. John Jones, for his inspiring and insightful advice. My thanks also go to Dr. Ash Parameswaran and Dr. Behraad Bahreyni for kindly serving on my thesis committee and providing valuable feedback that improves this thesis. This thesis would not have been possible without their strong support.

Many thanks to my best friends Lizzie Li and Peisong Guo. Although we are in different countries, you always provide sincere and unconditional support to me. I would also express my thanks to my SFU friends, they light my days in SFU.

Finally, and most importantly, I would like to express my indebtedness and the deep sense of gratitude to my parents, Suhua and Jihua, for their faith in me and allowing me to be as ambitious as I wanted. It was under their watchful eyes that I gained so much drive and an ability to tackle challenges head on. Also, I would like to thank Zicun Cong for his love that brightened my ordinary days. His support and encouragement were in the end what made this thesis possible.

Table of Contents

Approval ii

Abstract iii

Acknowledgements iv

Table of Contents v

List of Tables vii

List of Figures viii

List of Symbols x

List of Abbreviations xi

1 Introduction 1

2 Corona Discharge Ion beams Generator 6

2.1 Gas Discharge Mechanism 6

2.2 Gas Discharge Applications 12

2.3 Electron Beams Deflection 13

3 Discharge Tube Deflection Theory And Experiments 17

3.1 Ion Deflection in Vacuum 17

3.2 Ion Deflection in Low Vacuum 22

3.2.1 Drift-Drift Model 23

3.2.2 Drift-no collision Model 24

3.3 Limitation of Physical Models 24

3.3.1 Initial Velocity Limitation 24

3.3.2 Effects of Diffusion and Deionization 25

3.3.3 Space Charge Effect 26

3.3.4 Approximation on Electric Field Distribution 26

4 Experiments of Ion Deflections **29**
4.1 The Discharge Configurations 29
4.1.1 High Voltage Circuit and Load Resistor Technique 29
4.1.2 Output Signal Processing Module 30
4.1.3 The Vacuum Chamber 33
4.1.4 Magnetic Coil 35
4.2 Deflection Experiments 37
4.2.1 Discharge Device Structures 38
4.2.2 Ion Deflections vs. Magnetic Field 39
4.2.3 Ion Deflections vs. Discharge Distance 42
4.2.4 Ion Deflection vs. Discharge Current 44
4.2.5 Ion Deflections vs. Pressure 47
4.3 Discussion 50
4.3.1 Conclusion of Experiments 50
4.3.2 Signal Oscillation 52
4.3.3 Noise Analysis 54

5 Conclusion And Future Work **61**
5.1 Conclusion 61
5.2 Future Work 62

Bibliography **64**

List of Tables

Table 4.1 Comparison of SNR values at various discharge currents 58

List of Figures

Figure 1.1 Dual-cathodes corona discharge device structure 4
Figure 1.2 Top view of the ion beam gyroscope 5

Figure 2.1 I-V characteristics in the Townsend discharge regime 7
Figure 2.2 Paschen's Curve in the air 8
Figure 2.3 Four regions in a discharge tube 9
Figure 2.4 I-V characteristics in the glow discharge regime 9
Figure 2.5 The cathode ray tube 14
Figure 2.6 The second generation of the cathode ray tube used for deflection experiments 15

Figure 3.1 The corona discharge tube 18
Figure 3.2 The physical model derived for single ion in the discharge tube . . 18
Figure 3.3 The travel paths of ion in the crossed fields 20
Figure 3.4 Various ion paths at different magnetic fields in vacuum 21
Figure 3.5 The space charge effect 26
Figure 3.6 The non-uniform external electric field with the space charge effect 28

Figure 4.1 Experimental setup of ions deflection 30
Figure 4.2 Schematic diagram of the high voltage circuit. 31
Figure 4.3 Plot of typical gas discharge I-V showing various resistor loading lines. 32
Figure 4.4 Current to voltage conversion circuit and the DAQ 32
Figure 4.5 The outgassing level testing 34
Figure 4.6 Leakage testing at different outgassing levels 35
Figure 4.7 The two sets of coils were aligned for characterizing 36
Figure 4.8 Characteristics of the magnetic field and currents 36
Figure 4.9 The magnetic field uniformity of the two sets of coils 37
Figure 4.10 Photos of cathode layouts: (a) pin-plate and (b) pin-pin structure . 38
Figure 4.11 Influences of the magnetic field on ion deflections (Device 1) 40
Figure 4.12 Influences of the magnetic field on ion deflections (Device 2) 41
Figure 4.13 Influences of discharge distances on both discharge voltages and ions drifting fields 43

Figure 4.14 Relationship between ion deflection and discharge distances at 2 torr with both pin-pin device and pin-plate device 44
Figure 4.15 Influence of ion bombardments on cathodes: (a) before the gas discharge; and (b) after 80 hours of discharge 45
Figure 4.16 Ion deflections vs. discharge current at 2 torr 46
Figure 4.17 Ion deflections vs. discharge current at 5 torr 47
Figure 4.18 Comparison between ion displacement for divergent beam and converged beam 48
Figure 4.19 Discharge voltage with varied pressures at 12 μA 49
Figure 4.20 Ion deflections with pressure at various distances and discharge currents 49
Figure 4.21 Mechanism of corona discharge oscillations: (a) the conductor-to-ion configuration, and (b) the discharge tube with an electric field . . 53
Figure 4.22 Discharge current oscillations at 12 μA with Device A 55
Figure 4.23 Discharge current oscillations at 26 μA with Device A 56
Figure 4.24 Time series current signal at 12 μA with a corona oscillation period of 0.00242 s 57
Figure 4.25 Frequency domains power spectrum at 12 μA 58
Figure 4.26 Frequency domains power spectrum with various currents 59

Figure 5.1 The modified discharge device with a grid cathode and grounded cathodes 63

List of Symbols

I	Current
E	Electric field
σ	Air density factor
τ	Radius of curved pin
a_m	Magnetic acceleration
a_e	Electric acceleration
q	Electron charge
m	Mass of a single argon atom
B	Magnetic field
Ω	Speed of rotating
α_n	First Townsend ionization coefficient
d	Discharge distance
P	Gas pressure
V	Discharge voltage
R	Radius of cycloid path
y	Displacement
k	Boltzmann constant
T	Temperature
v	Velocity
D	Diffusion coefficient constant
K	Drift coefficient constant
R	Resistance
ϵ_0	Vacuum permittivity constant
S	Sensitivity
$Diff(\mu A)$	Differential current
$Def(\%)$	Deflection percentage

List of Abbreviations

MFP	Mean free path
CIV	Corona discharge inception voltage
ESP	Electrostatic precipitator
EHD	Eletrohydrodynamic
DLF	Direct-replacement laminar flow gun
DAQ	Data acquisition system
MUX	Multiplexer
PGA	Programmable-gain amplifier
ADC	Analog/digital converter
PCB	Printed circuit board
FFT	Fast Fourier transformation
SNR	Signal to noise ratio

Chapter 1

Introduction

The gyroscope is a sensor that measures the speed of a rotating platform. It has been widely used in aircraft, mobile phone and mining for the purpose of navigation [1]. Gyroscopes are based on different mechanisms, such as vibrating structure gyroscopes, fiber optic gyroscopes and thermal gyroscopes [2, 3, 4]. Most gyroscopes have area that can be improved. For example, the vibrating structure gyroscope has mechanical parts, which produces mechanical stress that affects its performance. The fiber optic gyroscope is expensive and huge in volume. And the thermal gyroscope has high signal interference induced by the gravity. In order to address these problems, we proposed an ion beam gyroscope that has no mechanical stress, no gravity interference and can be potentially optimized for low cost. The basic principle of the ion beam gyroscope is the deflection of ions by the Coriolis effect produced by a rotating platform, and by measuring the deflection magnitude of the ions, we can estimate the speed of the rotating. Coriolis effect was discovered by Coriolis in 1835, it produces an imaginary force called Coriolis force [5]. The Coriolis force is an inertial force that is acting on the right direction of a moving object on a rotating platform. It will result in an apparent displacement on the moving object, which is considered as Coriolis deflection. Inherently, there is no velocity or displacement along the angular direction of the moving object. It is the motion of the coordinate system that results in the deflection in the angular direction. The Coriolis acceleration produced by the Coriolis effect is [6]:

$$\vec{a}_c = -2\vec{\Omega} \times \vec{v} \tag{1.1}$$

where $\vec{\Omega}$ is the angular velocity vector, and $\vec{v}$ is the velocity of the beam source. In the later experiments, the magnetic field was used to emulate the effect of Coriolis effect. The Coriolis acceleration is in the right direction of the object movement, which is the same as the magnetic acceleration. And the Coriolis acceleration is proportional to the moving velocity of the object, which is also the same as the magnetic acceleration. Therefore, we can conclude that the magnetic field has the same effect on the ions as that of the Coriolis effect. Their relationship can be interpreted by the following equations.

The magnetic field is

$$\vec{F_m} = q\vec{v} \times \vec{B} \tag{1.2}$$

and the magnetic acceleration can be described as

$$\vec{a_m} = \frac{q\vec{v} \times \vec{B}}{m} \tag{1.3}$$

Substitute equation 1.1 into equation 3.13, we can correlate the angular velocity $\vec{\Omega}$ with the magnetic field

$$\vec{\Omega} = -\frac{q\vec{B}}{2m} \tag{1.4}$$

Using the magnetic field to emulate the Coriolis effect allows us to have a simpler experimental configuration, and magnetic field is easier to control than the speed of rotating. Consequently, it is advantageous to use the magnetic field to replace the Coriolis effect in the early exploring stage.

To explore the feasibility of the ion beam gyroscope, there are two challenges we are facing: 1.) how to generate a high quality ion beam with sufficient amount of ions; 2.) how to correlate the rotating speed with the deflection magnitude of ions. Inherently, both radioactive ionization and UV photoionization are widely used for ion beam generation. However, they can only produce a small current. A regular leak test of the radioactive source is required for radioactive ionization, and the UV equipment is huge and expensive. Consequently, the definitive method used for our ion beam generation is the corona discharge. The mechanism of it is to breakdown the gas electrically with a high electric field gradient around a high curvature electrode. Corona discharge can generate a reliable and sufficient current with simple and inexpensive setup, which is beneficial for us. Gas is a relatively good dielectric with bad electrical conduction. With the effect of a sufficient electric field, however, the movement of ionized gas particles driven by the electric field forms a conduction current. There are charged particles in gas created by natural processes, such as photoionization and radioactivity. With an external electric field, most electrical energy goes into charged particles. Those particles collide with and transfer energy to neutral molecules, which subsequently causes background gas ionization. Then, the generated ions and electrons are driven by the electric field for more collisions. As a result, avalanche occurs and enhances the current flow from femtoamperes to amperes. As one regime of the gas discharge, corona discharge can be obtained in a strong electric field with high curvature anode. The electric field is strong enough to ionize gas locally around a high curvature electrode. But it is insufficient to ionize neutral particles far away from the pin electrode, as the electric field drops dramatically with distance. Corona discharge is categorized into two types: positive corona discharge and negative corona discharge. For positive corona discharge, the curved pin electrode is connected to the high positive potential while plate electrode is grounded. In contrast, the opposite condition is applied to negative corona

discharge, of which curved pin electrode is connected to a high negative potential and plate electrode is grounded. The corona discharge inception voltage was firstly described by Peek's Law in 1929 as

$$E_c = \delta E_0 (1 + \frac{0.308}{\sqrt{\delta \tau}}) \tag{1.5}$$

where $E_0 = 31\ kV/cm$, δ is the air density factor with respect to SATP (25 °C and 760 torr), and τ is the radius of the curved pin in cm [7]. Following this work, researchers have derived more accurate formulas. For example, Meek's criterion explored semi-empirical theoretical criteria [8] and Nasser proposed a mathematical-physical model for corona streamer propagation and subsequent breakdown in a nonuniform field based on Meek's work [9].

For decades, corona discharge has received academic attentions from abundant applications in different realms [10]. For instance, it has been used in materials treatment [11], mass spectrometry [12], contamination removal [13], electron (ion) beam source in smoke detection [14], and pressure detection [15]. The performance of electron gyroscopes [16, 17] is limited by the earth's magnetic field interference. Hence, an elaborated shielding layer is required for the electron beam gyroscope, which is at a high cost. Since the charge to mass ratio of an ion is small compared to that of an electron, ion beam source is less sensitive to the earth's magnetic field. Consequently, it becomes important to explore the use of the corona discharge to generate a stable ion beam, and use Coriolis effect to deflect ion beams.

Since the relative effect of the ion beam deflection on a spinning platform by the Coriolis effect has not been explore, the relationship between the angular velocity and the ion deflection remains unclear. The exploration of ion beam sensors involves 3 steps: (1) Verify a measurable amount of ion beam deflection is detected; (2) Determine the correlations between deflection magnitude and magnetic field, and convert that into the relationship between deflection magnitude and angular velocity; (3) Figure out relevant parameters and their impacts on the performance of the ion beam sensor. Unlike the ion beam deflection, electron beams deflection by the magnetic field has been explored by many researchers to realize electron magnetometers. These magnetometers operate by detecting the effect of magnetic force [18, 19, 20]. The sensing principles are twofold: (1) The increment of the external magnetic field results in a change of current or voltage. By measuring the differential voltage (current), the corresponding magnetic field can be calculated. (2) Some magnetic sensors also use the phase shift of mechanical resonance caused by Lorentz force. For example, the most famous magnetometer based on Lorentz force is Hall effect sensor. Hall hypothesized a current flowing through a wire in a right-angle magnetic field got packed to one side of the wire. Hence, the crowding of the current produced a force to move the wire, and there was a slight but measurable differential voltage between two sides of the wire [21]. Based on this empirical hypothesis, Hall invented the Hall effect sensor to measure the magnetic field in 1879. It was later discovered that the differential voltage came from electron deflection by Lorenz force. Unlike the deflection of electrons, ions deflection by

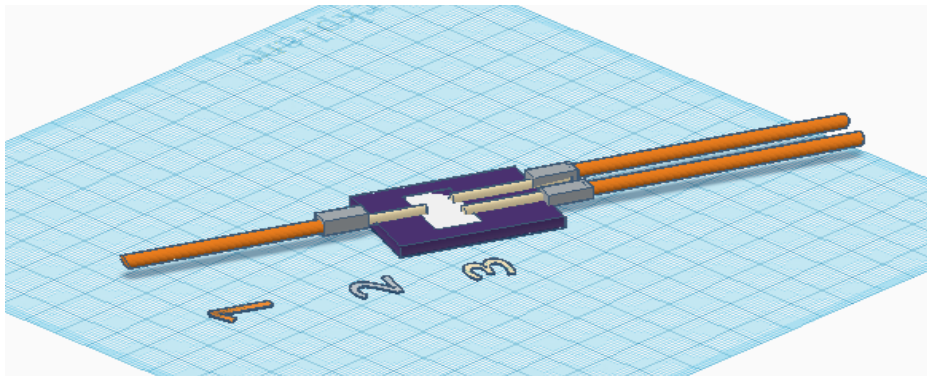

Figure 1.1: Dual-cathodes corona discharge device structure

magnetic fields has barely been recorded in the literature. However, we can speculate that Hall effect sensor is transferable to measure ion beam deflection, by detecting the differential signal caused by Lorentz force on ions. The smaller a magnetic field needed for a given speed ion beam source for a reasonable deflection magnitude, the smaller spinning effort is the rotating gyroscope and a better performance is the ion beam gyroscope. To achieve the simulated ion deflection by the Lorentz force, a dual-cathode discharge device is used to collect a differential current shown in Figure 1.1. The single pin is connected to a high positive voltage and the pair of identical cathodes are grounded. With the effect of corona discharge, ions drift to cathode are collected by different cathodes depending on their relative position. With the Coriolis effect, ions have probabilities to be deflected from one cathode to the other, which results in a differential current. As a result, a differential current correlates with a Coriolis force or a magnetic force. And the corresponding angular velocity can be estimated judging from the differential current.

In this thesis, we derived the theoretical model of ion movements in the discharge chamber. Then, experiments have been carried out to determine the relationship between angular velocity and differential current. Finally, the sensitivity of ion beam gyroscope was improved by optimizing relevant variables. The top view of the ion beam gyroscope is designed as shown in Figure 1.2

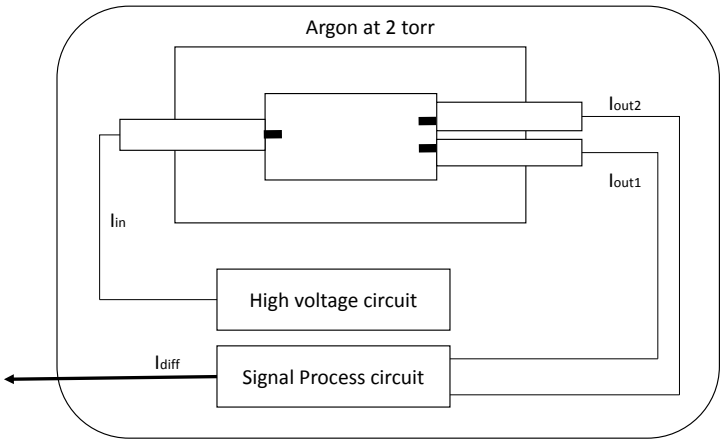

Figure 1.2: Top view of the ion beam gyroscope

Chapter 2

Corona Discharge Ion beams Generator

2.1 Gas Discharge Mechanism

Generally thousands of volts are required to break down a gas at atmospheric pressure. However, according to Paschen's curve, at a lower pressure, the electric field needed to break down gas reduces significantly. Since lower voltage is simple to achieve and operate, gas discharge under low pressure is favored in the exploration. Gas discharge consists of three regimes distinguished by the luminosity, and each regime has its unique I-V characteristics [22, 23, 24].

Townsend discharge

The current-voltage characteristics of Townsend discharge (Figure 2.1) were firstly found by Townsend [25]. When the applied electric field between two electrodes increases, the current increases proportionately at first and then stays as a constant I_0 referred as saturation current. When the applied voltage increases further, current increases exponentially. This phenomenon can be interpreted as the electron avalanche. When free carriers gain enough energy from the field, they collide with and transfer energy to neutral particles to produce more and more ionization. This region with exponentially increasing current is described by an equation

$$\frac{I}{I_c} = e^{\alpha_n d} \tag{2.1}$$

where I is the discharge current, I_c is the current leaving from cathode surface, d is the distance between electrodes, and α_n is the first Townsend ionization coefficient. α_n depends on the gas's physical properties, and those values can be found from the work of Townsend [25] and other subsequent literature [26, 27]. The voltage needed for electron avalanche inception is referred as breakdown voltage V_{bd}.

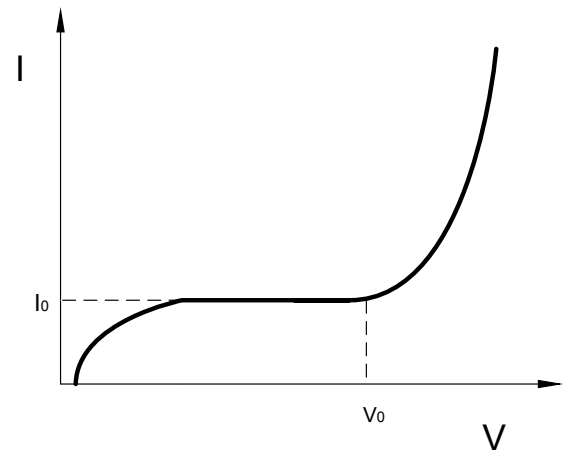

Figure 2.1: I-V characteristics in the Townsend discharge regime

Paschen [25] found that the breakdown voltage presents two regions with respect to the product of gas pressure p and discharge distance d between electrodes (Figure 2.2). The breakdown voltage is described by the following formula [25] according to Paschen:

$$V_{bd} = \frac{Bpd}{\ln(pd) + A} \tag{2.2}$$

where A and B are constant values derived from kinetic theory related to the characteristics of a given gas. To explain the appearance of the Paschen's valley, the term " mean free path" is introduced. Mean free path (MFP) is the distance a molecule travels before hitting other molecules. It is inversely proportional to the pressure. For air at atmospheric pressure, the MFP is about 96 nm. In the left side of the Paschen's valley, the product of the pressure and the distance (pd) is small. The MFP of the charged particles is relatively long compared to the distance d. Those particles gain sufficient energy but have few ionization collisions. Therefore, the breakdown voltage must be large enough to assure extreme high energy of gas molecules to start an avalanche. On the right side of Paschen's valley, however, the value of pd is large. Charged particles have a smaller MFP in this regime, which implies charged particles only have a shorter period to accumulate energy from the field. Thus, a higher breakdown voltage is needed for particles to gain sufficient energy.

In the Townsend discharge regime, current increases from femtoamperes to microamperes, and the saturation current is usually at the range of femtoamperes to picoamperes. Luminosity in this regime is very weak and light emitted is barely visible to human eyes.

Glow discharge

When the current increases further to milliampere range, discharge regime transits from Townsend discharge to glow discharge. A long cylinder tube is usually used as the discharge chamber to characterize glow discharge. As shown in Figure 2.3, the discharge gap is divided

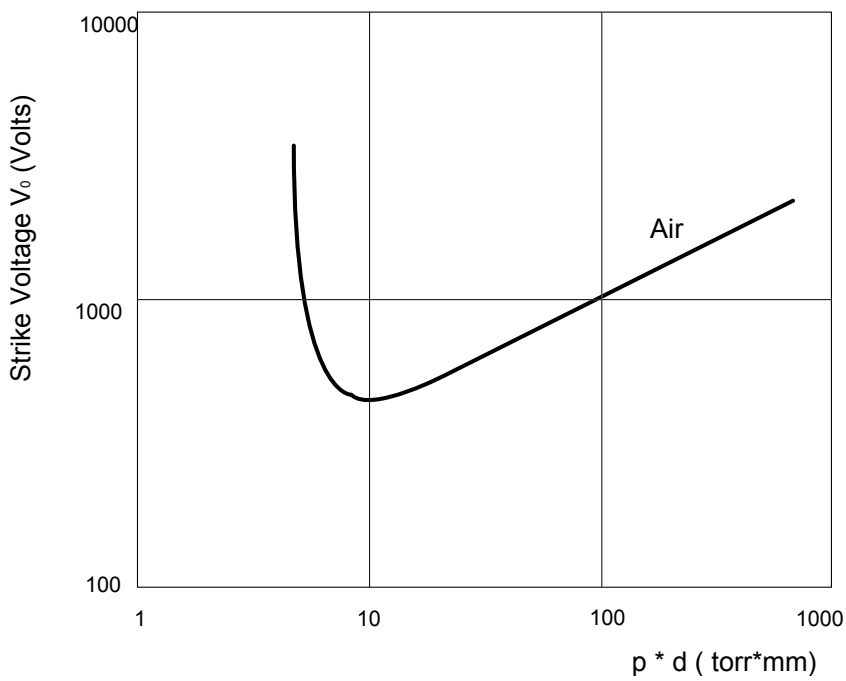

Figure 2.2: Paschen's Curve in the air

into four parts [28], and the relationship between the distance d and the electric potential Φ is also shown in this figure, which is non linear.

- Cathode Dark Spaces

  Electrons gain sufficient energy for ionization in this area. When atoms are ionized, the opposite charges are separated by the external electric field. As a result, the ion and electron pairs do not recombine immediately in this area. Since electrons tend to ionize rather than excite atoms, less excited atoms fall back to ground level emitting light. Thus, little visible light is produced in this area. [29].

- Aston Dark Space

  Electrons leave the cathode with a energy insufficient for ionization and excitation. This produces a thin dark layer next to the cathode.

- Negative glow

  Acceleration of the positive ions in the field leads to the secondary emission of electrons from cathodes to sustain the discharge. The recombination of ions and electrons into neutral molecules occurring in this region results in great light emission through a process called bremsstrahlung radiation [29]. This area remains the same in length when the discharge gap d increases.

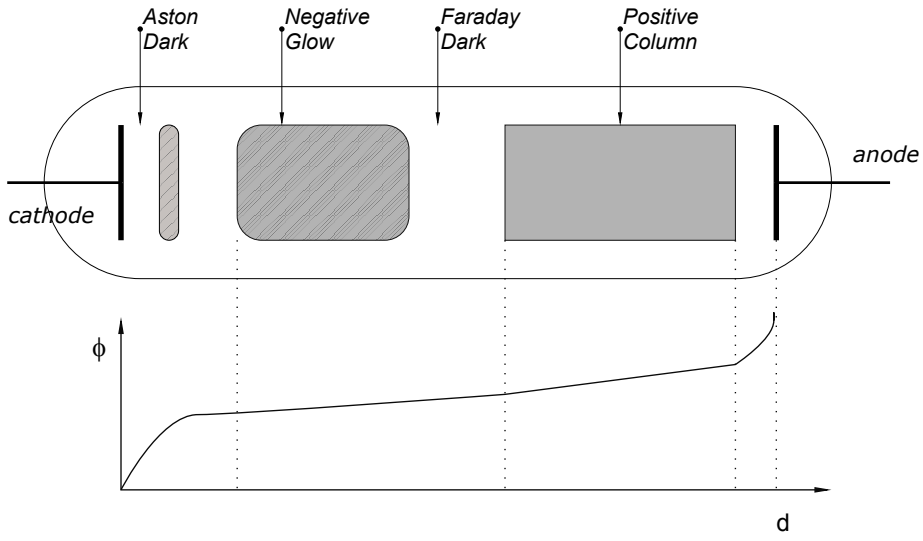

Figure 2.3: Four regions in a discharge tube

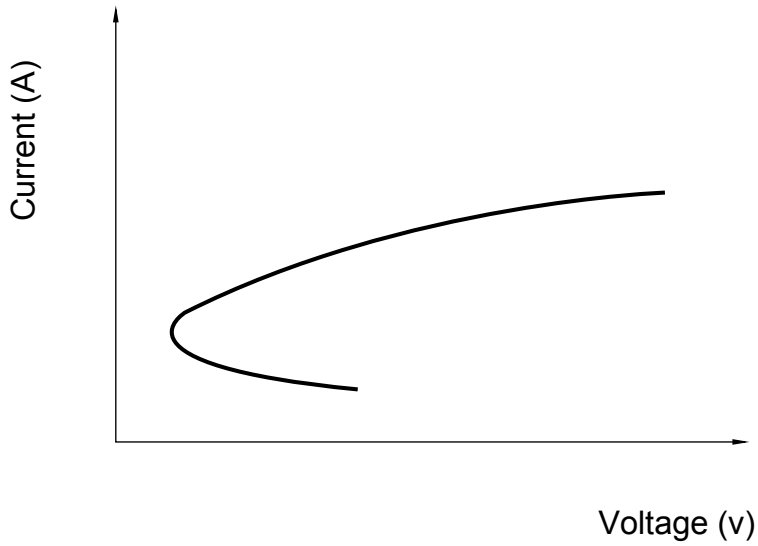

Figure 2.4: I-V characteristics in the glow discharge regime

- Faraday dark space

  This is the region that electrons or ions travel to gain enough energy for ionization collisions. The distribution of charged particles in the Faraday dark space is affected by ambipolar diffusion. It is less related to the external electric field [30], since the electric field gradient in this region is weak.

- Positive column

  The luminosity in this region is very high because of the great plasma density. When breakdown voltage approaches, a larger number of electrons, coming from secondary ionization, drift along the field and attach to neutral molecules. Consequently, heavy ions and charged atoms form a layer of plasma around the anode and cut off the current to the plasma sheath.

Glow discharge can be divided subsequently into abnormal glow discharge and normal glow discharge. In abnormal discharge region, voltage increases along with the increment of current, while normal discharge region (also called corona discharge) has a negative resistance. It has been identified that , if a pressure p of a given glow discharge, is in the left side of the valley of the Paschen's curve $pd < (pd)_{valley}$, it is located in the corona discharge regime, while $pd > (pd)_{valley}$ is believed to be in the normal discharge regime [31].

Corona discharge, by its definition, is a regime of gas discharge where the geometry confines the gas ionizing processes to high field ionization regions around the active electrodes [32]. One distinguishing feature of corona discharge is the low electric field drifting region, where charged particles are not able to gain sufficient energy for ionization collision because of the low electric strength. Pin-plate structure is preferred for corona discharge experiments, since a high curvature electrode allows a larger electric field for a given voltage. Gas molecules near the electrode get ionized because of the high electric field strength. The new formed "virtual electrode" - ionized molecules and the electrode itself (also known as electrode and the plasma region) becomes less sharp in field gradient.

Corona discharge inception voltage (CIV) is the voltage needed to initiate a corona discharge. Different from the breakdown voltage discussed above, the formula of the corona discharge inception voltage takes into consideration of the geometry parameters of the discharge device. CIV has received lots of attentions from researchers [9, 33, 34]. When CIV is reached, the electric field on the pin electrode surface is E_c and a bright plasma layer is visible at a radial distance from the electrode before the electric gradient goes down to the gas breakdown field gradient E_v. CIV can be described by the formula

$$E_c = m_0 E_v r ln(\frac{d}{r}) \tag{2.3}$$

where $E_v = E_0\delta(1 + \frac{c}{\sqrt{\delta r}})$ is the corona inception voltage gradient. E_0 is the disruptive electric field, and $E_0 = 3 \times 10^6\ V/m$ in air at STP, $\delta = \frac{\rho}{\rho_{(STP)}}$ is the air density factor, c is

an empirical dimensional constant considered as 0.301 $cm^{1/2}$, r is the radius of the discharge pin tip, d is the distance between discharge electrodes, and m_0 is the roughness of discharge pin electrode. For polished pin $m_0 = 1$, while for roughened pin $m_0 = 0.98 - 0.93$.

Corona discharge can be classified into two types depending on the polarity of the field applied.

1. Positive discharge

   The positive corona discharge requires a positive voltage on the pin electrode and a grounded potential for the other electrode as the cathode. The positive discharge starts with burst pulse corona locally around the pin anode because of the high electric potential gradient. Electrons ionized by natural processes move to the curvature anode while positive ions are repelled by the anode. This natural process can be described as

   $$A^* + hv \rightarrow A^+ + e^- \tag{2.4}$$

   where A^* represents the atom in an excited state. With sufficient energy gaining from the electric field, electrons complete ionization collisions with neutral molecules. This ionization process is described by the formula

   $$A^m + B \rightarrow A^+ + B + e^- \tag{2.5}$$

   Where A^m is a molecule in metastable states that has an extended lifetime to seconds because of excited electronic states. The secondary electrons generated in this process are attracted to the plasma region around the anode. Thus, the anode is surrounded by high energy electrons, and avalanches exist in the plasma region.

2. Negative discharge

   For negative discharge, a negative voltage is applied to the pin electrode, while the planar electrode is served with grounded potential. Its physical phenomenon is similar to positive discharge at the beginning. It starts with natural ionization of primary electrons and positive ions. Ions generated are attracted to the curvature cathode and form a primary plasma region around the electrode. Then, ions in the plasma region release high energy photons from the relaxing process. Since the energy of photons is larger than the work function of electrode material, electrons are emitted from electrode after absorbing photon energy. Escaped electrons are repelled from the curvature cathode, forming secondary electrons avalanches. This process is called photoelectric effect and can be illustrated by

   $$e^- + A \rightarrow A^* + e^- \tag{2.6}$$

   $$A^* \rightarrow A + hv \tag{2.7}$$

$$hv > e\phi \tag{2.8}$$

where ϕ is the work function of an electron of the electrode material.

The positive corona discharge and the negative corona discharge are similar in two aspects: (1) high energy positive ions or metastable particles bombard the electrode, and this interaction results in a secondary emission of two electrons, one of which neutralizes the positive ion while the other electron becomes a free carrier; (2) electrons inside the electrode gain sufficient energy from the violent thermal lattice vibrations to escape from the material binding [35], and this process dominates in hot electrode discharge particularly.

If the discharge current increases further, the normal discharge ends and transits to the abnormal discharge. Current becomes tremendous at this moment, and thermal ionization is important in generating secondary electrons (ions). Glow covers more and more inter-electrodes area. Unlike corona discharge, the abnormal discharge has a positive resistance. A greater current corresponds to a larger discharge voltage. Current exponentially increases to a few amperes in the abnormal discharge regime. This may have a bad effect on the durability of electrodes because of the plasma etching.

Arc discharge

The arc discharge has a negative resistance. Gas discharge in this regime is distinguished by its high temperature. Thermionic emission of the secondary electrons from cathode materials becomes the major cause of electron avalanche. High-field emission also plays an importance part because of cathode spot effect [36]. Fizz sound and a large amount of radiation are produced.

2.2 Gas Discharge Applications

Every regime of discharge is valuable. The Nixie tubes, decatrons, neon lamps use the glow discharge regime for displays and lighting. Arc discharge regime are not only used for industrial welding and furnacing, but also used for high voltage switch gears in high voltage transmission networks [37].

The most popular and promising application of gas discharge is to use corona discharge to generate ion beams.

- Electrostatic Precipitators

  An electrostatic precipitator (ESP) is a filtration device that removes or collects particulate emissions, such as dust and smoke from a given gas flow using the force of an induced electrostatic charge minimally impeding the flow of gases through the unit [38]. Each ESP layer contains a planar plate and a corona wire. The plate is connected to a kilo-volt positive voltage while the corona wire is grounded. The plate

and wire are placed next to each other in a small distance, which is favored for corona discharge. When a gas flow with dust particles goes into ESP system, dust particle will be charged and collected by the plate because of the electrostatic force. ESP is widely used in building ventilation systems for improving the indoor air condition [39].

- Plasma Reactors and Sputtering

  The development of high DC voltage gas discharge has a dramatic influence on the energy at which ions interacting and impinge on the electrode or on a substrate lying on the electrode [40]. Corona induced plasma reactors are widely used to promote oxidation, chemical reaction, and etch away highly anisotropic area of the substrate.

- Sensors

  The current-voltage characteristics of corona discharge have been noticed to be altered with different operating pressure. Consequently, pressure sensors have been developed based on corona discharge. The older generation of radioactive smoke detector has been substituted gradually with gas discharge smoke detector for safety reason [41]. Its principle is that corona discharge generates a continuous and stable beam source to form a current. If dusts or smoke particles exist, the carriers' density decays in magnitude, causing a decrease in the current. An electrohydrodynamic (EHD) device is invented based on Newton's third law of motion [42]. The ion beam source transfers momentum to neutral particles on their way. So the EHD device is thrusted in the opposite direction of the ion flows.

Previous work has proved corona discharge is an excellent ion beam source for sensors. Therefore, exploring whether corona discharge is applicable for gyroscope is with value.

2.3 Electron Beams Deflection

The electron beam deflection has been explored by many researchers [43, 28]. Since the electron has small charge to mass ratio, it responses significantly to electromagnetic force. Devices, such as the display panel and magnetometers have been invented based on this characteristic. One of the most famous electron beam deflection experiments is the "cathode ray tube" invented by German physicist Ferdinand Braun and J.J Thomson coincidentally in 1879 [43]. The cathode ray tube (Figure 2.5) is a low-pressure gas discharge tube with two planar electrodes. The low-pressure configuration has two advantages: (1) It has a low breakdown voltage to generate sufficient electrons ; (2) It has a large MFP for an electron to gain enough energy from the field. Electrons produced by background gas ionization and cathode material emission drift towards the anode. Some electrons are collected by the electrode, while the majority escapes the cathode area because of the great velocity [28].

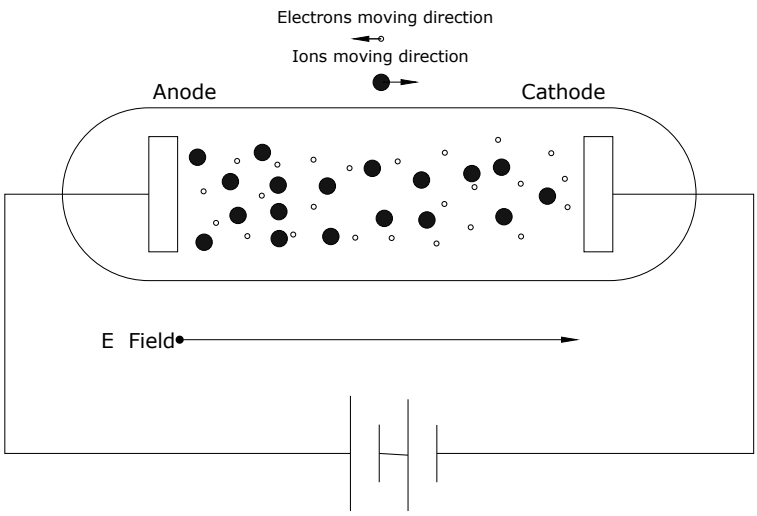

Figure 2.5: The cathode ray tube

When a magnetic field is at right angle to the electrons' velocity, electrons will bend their paths due to electron deflection by the Lorentz force.

The second generation of the cathode ray tube has been developed subsequently with different configurations. One type of the second generation cathode ray tube is the direct-replacement laminar flow electron gun configuration (Figure 2.6). Direct-replacement laminar flow gun (DLF) is favorable for producing a stable and uniform cylinder electrons source. A typical DLF cathode ray tube is divided into four fundamental regions.

- Electron Generation Region

  Numerous electrons are generated by gas discharge in this region. Some electrons strike the electrode and lose their energy, but most electrons shoot over and escape from the discharge area. Grid 1 is a pair of electrodes with several kilo-volt for accelerating electron beams. The downside of having grid 1 is the causing of gas discharge cut-off to the previous stage. However, this can be addressed by having another pair of grids as the secondary anode. The secondary anode usually has a voltage of a couple of hundred volts to make grid 1 a lower cut-off voltage. Generally, the spacing between two anodes (grid 1 and grid 2) is small to avoid space charge effect and prevent beams from diverging.

- Electron Focusing Region

  Focusing region plays an important part in improving the resolution of electron display. In this region, beams are converged by an external force. Both the magnetic field and the electrostatic field are widely used to serve the purpose. Figure 2.6 shows the

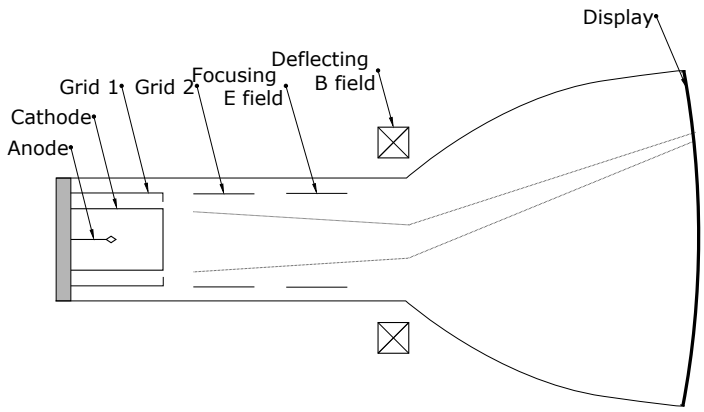

Figure 2.6: The second generation of the cathode ray tube used for deflection experiments

use of the electrostatic method to focus the beam. A pair of electric plates with the same potential is used so that electrons are converged with little loss of current (beam source).

- Electron Deflection Region

  Although electric field can also be used, Figure 2.6 uses a magnetic field to deflect electron beams. This is realized by making use of the magnetic coil surrounding the neck of the cathode ray tube. By varying the current in the coil, different deflection amplitude can be obtained. The deflection amplitude is proportional to the current flowing through the magnetic coil within this region.

- Electron Drifting Region

  Drifting region is a power free area that allows electrons to continue their paths freely. There are few collisions and electrons will eventually strike the display screen to lighten a dot. In this region, electron beams are inclined to diverge a little bit due to Coulomb's force and space charge effect.

Different from the development of the electron deflection, the study of ion beam deflection in a setup similar to cathode ray tube is completely inadequate. However, mass spectrometer employs ion beam deflection but with a different structure. The mass spectrometer is an instrument to identify an ion's charge to mass ratio by deflecting it with a magnetic field. While cathode ray tube is usually small, mass spectrometers are great in size. And mass spectrometers tend to have fairly high vacuum. Similarly to the cathode ray tube, mass spectrometer includes four basic regions.

- Ionization Region

Electron gun is used to generate high energy electrons and ions. Then, electrons get trapped by an electron cage in this region. As a result, only ions escape out of this area. The escaped ions are orientated (by the repelling force) and initially accelerated by a planar plate with positive potential.

- Acceleration Region

  Ion beams entering this region travel between a set of charged parallel plates. Ions are repelled by one plate and attracted to the other. There is only a narrow slit cut between each set of plates which converges ion beam in a very focusing path at the accelerated rate. Unlike using the same potential plates in cathode ray tube for reducing the loss of electrons, complementary plate pairs are used to provide an accelerating force while ion beams are converged by the geometrical structure - the narrow slit.

- Deflection Region

  The deflection region must be great enough to assure a measurable amount of deflection. This makes it difficult to shrink the size of the mass spectrometer. Ions with a smaller charge to mass ratio have a smaller deflection magnitude for a given field. Consequently, the charge to mass ratio can be determined by judging from the deflection magnitude.

- Detection Region

  Detectors are separated on the collecting plate spacing by narrow gaps. Ions with different charge to mass ratios get captured by different detectors. Each detector corresponds to a certain charge to mass ratio.

The downsides of the mass spectrometer are threefold. (1) The vacuum level of this instrument has to be significantly high (in milliTorr range) to assure no collision between ions and background gas molecules outside the ionization region. (2) Great distance is demanded for a significant amount of ion deflection. Distance shifting in y axis implies the magnitude of the ion deflection. (3) The acceleration region requires an extra power supply of kilo-volt, which asks for more complicated high voltage circuit. This instrument demonstrates that heavy ions (compared with electrons) can be deflected in a measurable amount under low pressure, although a great deflection region and extremely low pressure are needed.

To address the downsides of the mass spectrometer, a simpler and more compact structure is proposed to explore the ion deflection. And magnetic field is directly applied to the device in the beam generation region. If a moderate deflection can be achieved in the new setup, an ion beam gyroscope might be applicable.

Chapter 3

Discharge Tube Deflection Theory And Experiments

3.1 Ion Deflection in Vacuum

The study of physical phenomena inside the discharge tube is essential to investigate the motion of ions. For a typical discharge tube (Figure 3.1), the discharge distance between anode and cathode is d, and the voltage drop across is V. A magnetic field $\vec{B}$ is at right angle to the electric field $\vec{E}$. The anode is a high curvature pin electrode and the cathode is a planar plate with a length of L_0. L_0 is much smaller compared to the discharge distance d ($L_0 \ll d$). The structure allows a positive corona discharge. A simplified physical model in this discharge tube is shown in Figure 3.2.

It will be easier to start with the single ion motion in the discharge tube. Assuming only one ion is excited from the natural process, and it will drift along the electric field. If pressure inside the chamber is sufficiently low, this ion will not collide with other molecules. If a magnetic field is applied at right angles to the electric field, the ion will be affected by both electric and magnetic fields. Equations have been built up to monitor the motion of the ion in the crossed fields. Since the ion is released from rest, it has an initial velocity of 0. The resultant force on it can be described by the formula

$$\vec{F} = q(\vec{E} + \vec{v} \times \vec{B}) \tag{3.1}$$

In the x axis,

$$F_x = m\frac{dv_x}{dt} = qv_yB + qE \rightarrow \frac{dv_x}{dt} = \frac{qBv_y}{m} + \frac{qE}{m} \tag{3.2}$$

And in the y axis,

$$F_y = m\frac{dv_y}{dt} = qv_xB \rightarrow \frac{dv_y}{dt} = \frac{qBv_x}{m} \tag{3.3}$$

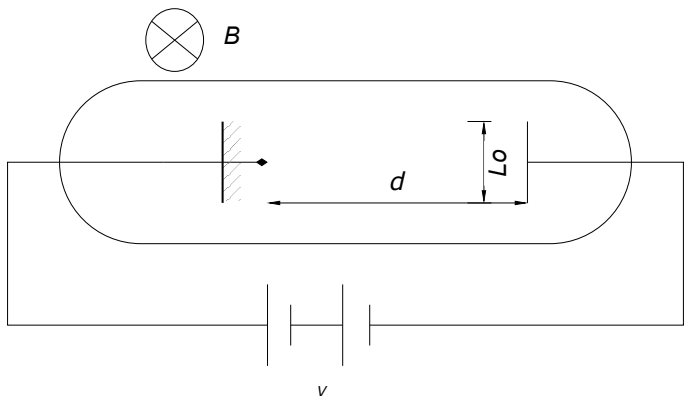

Figure 3.1: The corona discharge tube

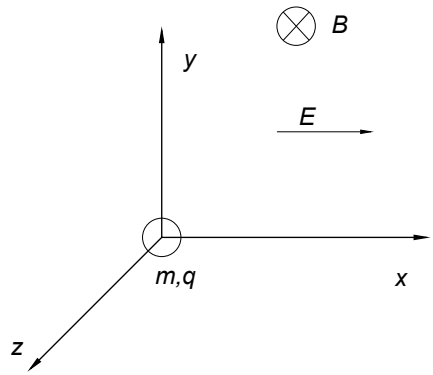

Figure 3.2: The physical model derived for single ion in the discharge tube

Therefore

$$\frac{d^2v_y}{d^2t} = \frac{qB}{m}\frac{dv_x}{dt} \tag{3.4}$$

Substitute equation 3.2 into 3.4

$$\frac{d^2v_y}{d^2t} = \frac{qB}{m}(\frac{qBv_y}{m} + \frac{qE}{m}) \tag{3.5}$$

The initial condition is $v_x(0) = v_y(0) = 0$. Substitute the equation 3.1 into 3.4 to solve the differential equation. The v_x and v_y of the ion are:

$$\begin{aligned} v_x(t) &= \frac{E}{B}sin(\frac{qBt}{m}) \\ v_y(t) &= \frac{E}{B}(cos(\frac{qBt}{m}) - 1) \end{aligned} \tag{3.6}$$

The position of the particle at time t is:

$$x(t) = \frac{E}{B}\int(sin(\frac{qBt}{m})dt = \frac{Em}{qB^2}(1 - cos(\frac{qBt}{m})) \tag{3.7}$$

$$y(t) = \frac{E}{B}\int(cos(\frac{qBt}{m}) - 1)dt = \frac{Em}{qB^2}sin(\frac{qBt}{m}) - \frac{Et}{B} \tag{3.8}$$

Unlike the path in the cathode ray tube or mass spectrometer, the motion of the ion in the compact discharge tube forms a cycloid path in the plane as shown in Figure 3.3, and the diameter of the cycloid along the y is $S = \frac{2\pi mE}{qB^2}$.

The radius of the cycloid path is $R = \frac{2mE}{qB^2}$. By substituting certain experimental parameters, we are able to estimate the approximate R value for our experimental condition. For example, argon gas is used in the electrical gas discharge experiment, therefore, m is the mass of the argon atom which equals to 6.63×10^{-26} kg [44]. q is an electron charge $= 1.60217662 \times 10^{-19}$ C. The discharge voltage V ranges from 300 to 600 volts and the discharge distance ranges from 2 mm to 20 mm. As a result, the electric field can be calculated

$$E = \frac{V}{d} = 1.5 \times 10^4 - 3 \times 10^5 V/m \tag{3.9}$$

As B is the magnetic field intensity which is between 0.01 and 0.001 T, its corresponding spinning rate for providing the same amount of Coriolis force to replace magnetic field can be described as

$$\Omega_{max} = \frac{qB}{2m} = \frac{1.602 \times 10^{-19} \times 0.01}{2 \times 6.63 \times 10^{-26}} = 1.2 \times 10^4\ rad/s. \tag{3.10}$$

and

$$\Omega_{min} = \frac{qB}{2m} = \frac{1.602 \times 10^{-19} \times 0.001}{2 \times 6.63 \times 10^{-26}} = 1.2 \times 10^3\ rad/s. \tag{3.11}$$

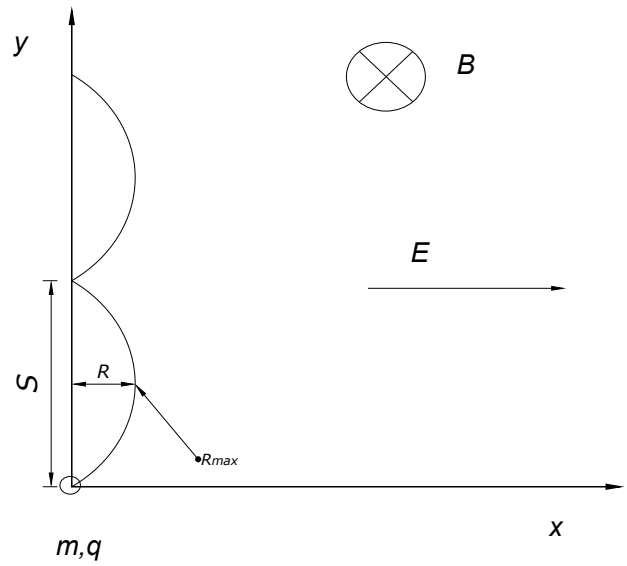

Figure 3.3: The travel paths of ion in the crossed fields

Hence, the angular velocity of the spinning frame is in the range of 1×10^3 to 1×10^4 rad/s so as to provide a Coriolis force with the same order of magnitude as the magnetic force.

Substituting the above values into the equation $R = \frac{2mE}{qB^2}$, R is estimated to have its minimum value of

$$R_{min} = \frac{2 \times 6.63 \times 10^{-26} \times 1.5 \times 10^4}{1.602 \times 10^{-19} \times (0.01)^2} \approx 124\ m \tag{3.12}$$

This value is larger than the discharge distance $d \ll R$. Therefore, the ion arrives at cathode before it reaches the peak of the cycloid path. Figure 3.4 shows the ion paths at various magnetic fields ($B_0 > B_1 > B_2$). The ion is released from anode at $x = 0$ with a velocity $v_0 = 0$. It follows the cycloid path and arrives at the cathode area (dotted line). Therefore, the ion only travel a small segment of the cycloid path. The ion might rush out of the discharge region ($0 < x < d$) to the cut off region ($x > d$) and continues its path with no external force.

For a discharge tube with a discharge distance of d, ion travels d in the x axis. Substitute $x(t) = d$ into the equation 3.8 to estimate distance displacement in the y axis $y(d)$,

$$y(d) = \frac{Em}{qB^2}[sin(cos^{-1}(1 - \frac{dqB^2}{Em})) - cos^{-1}(1 - \frac{dqB^2}{Em})] \tag{3.13}$$

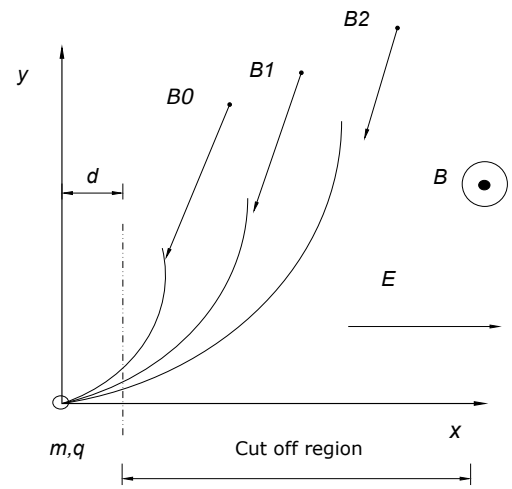

Figure 3.4: Various ion paths at different magnetic fields in vacuum

In order to find out a more clear relationship between distance displacement $y(d)$ and magnetic field B, small angle approximation has been introduced to simplify this complicated equation. Assume,

$$cos(\theta) = 1 - \frac{dqB^2}{Em} \tag{3.14}$$

The maximum value of the second term $\frac{dqB^2}{Em}$ is

$$\frac{dqB^2}{Em} = \frac{20 \times 10^{-3} \times 1.6 \times 10^{-19}(0.01)^2}{\frac{300}{20\times10^{-3}} \times 6.63 \times 10^{-26}} \approx 3.22 \times 10^{-4} \tag{3.15}$$

Therefore, $cos(\theta)$ can be taken as ≈ 1, and θ is a small angle. In a small angle approximation,

$$cos(\theta) \approx 1 - \frac{(\theta)^2}{2} \tag{3.16}$$

Then,

$$cos(\theta) = 1 - \frac{dqB^2}{Em} \approx 1 - \frac{(\theta)^2}{2} \tag{3.17}$$

and

$$\theta = (\frac{2dq(B)^2}{Em})^{1/2} \tag{3.18}$$

Therefore, the original equation 3.13 can be simplified as

$$y(d) = \frac{Em}{qB^2}[sin(\theta) - \theta] \tag{3.19}$$

The small angle approximation can also be applied to sin function,

$$sin(\theta) = \Sigma \frac{(-1)^n}{(2n+1)!}\theta^{2n+1} \tag{3.20}$$

Taking the first two most significant term, it becomes

$$sin(\theta) \approx \theta - \frac{(\theta)^3}{3!} \tag{3.21}$$

Finally,

$$y(d) = \frac{Em}{qB^2}(-\frac{(\theta)^3}{6}) \tag{3.22}$$

By substituting the formula 3.18 into 3.19,

$$y(d) = -\frac{Em}{qB^2}(\frac{((\frac{2dq(B)^2}{Em})^{1/2})^3}{6}) \tag{3.23}$$

Therefore,

$$y(d) = -\frac{EmB}{6q}(\frac{2dq}{Em})^{3/2} \tag{3.24}$$

Since

$$E = \frac{V}{d} \tag{3.25}$$

In equation 3.24, substitute 3.25 to replace E

$$y(d) = -\frac{\sqrt{2}B}{3}(\frac{q}{Vm})^{1/2}d^2 \tag{3.26}$$

With reasonable approximation, we can conclude that $y(d)$ is proportional to magnetic field B and square of the discharge distance d^2, and it is inversely proportional to the square root of the discharge voltage $\sqrt{V}$.

3.2 Ion Deflection in Low Vacuum

Since it is difficult to obtain gas discharge in vacuum with a small supply voltage, a low vacuum level of 1-10 torr is introduced in a practical case. As a result, the former model in vacuum is no longer valid because of interaction between ion and neutral particles.

Since argon is used as discharge gas, the MFP for argon from 1 to 10 torr is approximately 48 μm to 4.8 μm respectively [45]. In my experiments, the discharge distance d is always larger than 2 mm, which is larger than the MFP. Consequently, there will be many collisions in the x axis before the ion arrives at the cathode area. As for the y axis, given that

$$y(d) = (-\frac{\sqrt{2}}{3})\sqrt{\frac{q}{Vm}}d^2B \tag{3.27}$$

Substitute parameters with their value ranges, the minimum value of the distance displacement in the y axis is

$$ymin(d) = 0.12\ \mu m \tag{3.28}$$

which is smaller than the MFP $(48 - 4.8)\ \mu m$ in the given pressure range. In this case, the ion collides with background gas only along the x axis. However, the maximum value of the distance displacement in the y axis is

$$ymax(d) = 169\ \mu m \tag{3.29}$$

which is larger than the minimum MFP. Therefore, collisions between the ion and neutral particles might exist in both directions.

Consequently, we derived two models to predict the motion of the ion in different cases. (1) Drift-drift model is applied to the case when $d > MFP$ and $y(d) > MFP$, so the ion collides with other molecules in both the x axis and the y axis. (2) Drift-no collision model is valid when $d > MFP$ and $y(d) < MFP$, where collisions only appear on the x axis.

3.2.1 Drift-Drift Model

The drift velocity is affected by the pressure condition of the discharge system since the ion will interact with other molecules in both axes. Drift velocity has been found out to have a segmented relationship with E/p. Three regions are readily identified.

1. For a great value of E/p, the velocity v approaches a straight line with a slope of $\frac{1}{2}$, which indicates that $v \propto (E/P)^{\frac{1}{2}}$. In this region, thermal energy is negligible compared to the energy gained from the strong field, and the velocity distribution of ions was studied by Wannier [46].

2. For a small value of E/p, the velocity has a tendency to a line with a slope value of 1, which implies that $v \propto (E/p)$. As a result of energy interaction thermally, the velocity distribution is known as Maxwellian function in this region [47].

3. A transition region at an intermediate value of E/p connects the other two regions.

For argon, when $E/p > 100\ V/cm{\cdot}torr$ at room temperature, it is in the high field region ($v \propto (E/P)^{\frac{1}{2}}$), and when $E/p < 50\ V/cm \cdot torr$, it is in the low field region ($v \propto (E/p)$) [47]. In my exploration, the electric field is designed from 150 to 3000 V/cm and pressure is from 1 to 10 torr. Therefore, the corresponding E/p ranges from 15 $V/cm \cdot torr$ to 3000 $V/cm \cdot torr$.

Replace E with $g(E/p)$ to integrate the impact of pressure, and the equation 3.6 becomes:

$$\begin{aligned} v_x(t) &= \frac{g(E/p)}{qB}\sqrt{\frac{P}{k_0}}sin(\frac{qBt}{m}\sqrt{\frac{k}{P}}) \\ v_y(t) &= \frac{g(E/p)}{qB}(cos(\frac{qBt}{m}\sqrt{\frac{k_0}{P}}) - 1) \end{aligned} \tag{3.30}$$

where $g(E/p)$ is the function that describes the relationship between the drift velocity v and E/p. $g(E/p)$ is a piecewise function. When $E/p < 50\ V/cm \cdot torr$, it equals to $g(E/p) = c_0(E/p)$, and when $E/p > 100\ V/cm \cdot torr$, it is $c_1(\frac{E}{p})^{1/2}$.

3.2.2 Drift-no collision Model

The ion only interacts with particles in the x direction while it travels in a quasi-vacuum with no collision along the y direction. Therefore, pressure changes the drift velocity in the x axis. According to figure 3.4, figure 3.3 and equation 3.12, the displacement in the x axis of the ion is $d = 0.02\ m$ while the radius of the cycloid path is $R_{min} = 124\ m$. The ion arrives at cathode in a short time, and electric force is considered to be much larger than the magnetic force. Therefore, we ignore the effect of magnetic force on the drift velocity. The motion of the ion is formulated as

$$\begin{aligned} v_x(t) &= \frac{g(E/p)}{qB}sin(\frac{qBt}{m}) \\ v_y(t) &= \frac{g(E/p)}{qB}(cos(\frac{qBt}{m} - 1)) \end{aligned} \tag{3.31}$$

3.3 Limitation of Physical Models

Approximations were used during the modelling process. As a result, there is a small bias between the approximated model and the realistic model.

3.3.1 Initial Velocity Limitation

Each ion was considered as released from rest, so its initial velocity was zero. However, ions are generated from the gas discharge, so each ion remains in thermal equilibrium before it is accelerated by an external field. Assuming an even distribution of temperature, the average energy of one ion is

$$\frac{1}{2}mv_{eff}^2 = \frac{3}{2}kT \tag{3.32}$$

where m is the respective mass of an ion and v_{eff} is the corresponding velocity at given temperature T, and k is the Boltzmann constant $1.38 \times 10^{-23} J \cdot K^{-1}$ [48]. Therefore, the

velocity of an initially released ion is

$$v_{eff} = \sqrt{\frac{3kT}{m}} \tag{3.33}$$

However, each ion has a random direction. If there is only one ion generated from the discharge process, the velocity of this ion is described by equation 3.33 , and its direction is uncertain. In fact, the gas discharge produces so many ions from stochastic process that the net velocity of the ion beam can be taken as zero. As a result, this approximation would not influence the accuracy of the theoretical model.

3.3.2 Effects of Diffusion and Deionization

Ions are produced around anode and move to the cathode in the discharge tube, which makes the concentration spatially non-uniform. Ions will diffuse from higher concentration region to lower concentration to achieve an equilibrium. This process leads to a diffusion velocity caused by the ion concentration gradient. Generally, negative ions have a higher diffusion velocity, and the differential rate of diffusion between negative ions and positive ones will build up an internal electric field. The field consequently tends to augment the drift velocity of positive ions and retard negative ions. As a result, the drift velocity is not only affected by external electric and magnetic fields, but also by internal electric field built up by the diffusion process [24]

$$v_x = F_0(E) + F_1(B) - \frac{D^+ d_n^+}{n^+ d_x} \tag{3.34}$$

The internal E field is [24]

$$E_{inter} = -\frac{D^- - D^+}{K^- + K^+} \frac{1}{n} \frac{dn}{dx} \tag{3.35}$$

where D is the diffusion coefficient constant, F_i is the effect of electromagnetic fields. dn/dx is the concentration gradient of ions and K is the drift coefficient constant.

Deionization process is simultaneous with ionization process in the discharge tube. Therefore, it is necessary to analyze this process. Two deionization mechanisms have been studied by Kuffel [24].

1. Recombination

   Electrons and ions combine and their potential energy releases as quantum of radiation.

   $$A^+ + e \rightarrow A + hv \tag{3.36}$$

2. Attachment

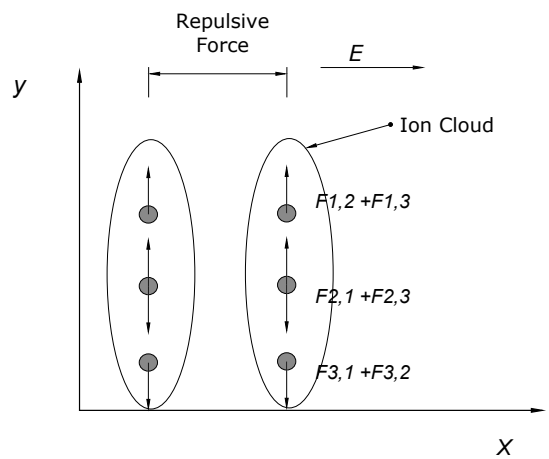

Figure 3.5: The space charge effect

Neutral molecule captures one electron to form a negative charged ion and release excess energy by releasing as quantum.

$$A + e \rightarrow A^{-} + hv \tag{3.37}$$

Therefore, the contribution of diffusing process should be taken into account in modeling the drift velocity.

3.3.3 Space Charge Effect

Space charge effect is a result of mutual repulsion of particles in the discharge tube, which limits the current of the ion beam. And it can also cause some motion of ions in a beam or packet in addition to that caused by external fields [49]. As a result, the original ion beam is prone to diverge during its propagation to the cathode. Figure 3.5 is the simplified explanation of the space charge effect.

Every pair of ions has a mutual Coulomb repulsive force. So ions are pushed away to form a divergent beam. One ion travels further than the formula 3.8 described in the y axis because of this force. In the x axis, ions forms a plasma region, which repels coming ions backwards. And this effect presents an oscillation pattern at the output stage in corona discharge regime.

3.3.4 Approximation on Electric Field Distribution

The external electric field was considered as a uniform electric field across the whole ion propagation region, which is not accurate for corona discharge with pin-plate and pin-pin

configurations (Figure 3.6). Taking pin-plate structure as an example, due to the planar shape of cathode, electric field diverges with a small angle θ as shown in Figure 3.6.

$$cos(\theta) = 1 - \frac{L_0^2}{2d^2} \tag{3.38}$$

As a result, ions at different positions may have varied acceleration rates. In my experiments, the discharge distance d has a range from 0.002 m to 0.02 m and the length of the planar plate L has a range from 0.0001 m to 0.001 m. Hence, we can estimate the range of θ.

$$\frac{1}{2}\frac{0.0001}{0.02} \leq tan(\frac{\theta}{2}) \leq \frac{1}{2}\frac{0.001}{0.002} \tag{3.39}$$

Therefore,

$$0.005 \leq \theta \leq 0.5 \tag{3.40}$$

The error is

$$error = \frac{Ecos(\frac{\theta}{2}) - E}{E} = 1 - cos(\frac{\theta}{2}) \tag{3.41}$$

Substitute the range 3.40 into 3.41, we can get the error of this approximation:

$$0.0003\% \leq error \leq 3.1\% \tag{3.42}$$

As a result of, the overall electric field is not spatially uniform. And the potential gradient near the anode is much greater than in other areas. Figure 2.3 provides the potential distribution inside a typical discharge tube. Therefore, the internal physical phenomena also add errors and difficulties in getting an accurate theoretical model. Consequently, a trade-off between the modelling effort and the modelling accuracy has been applied.

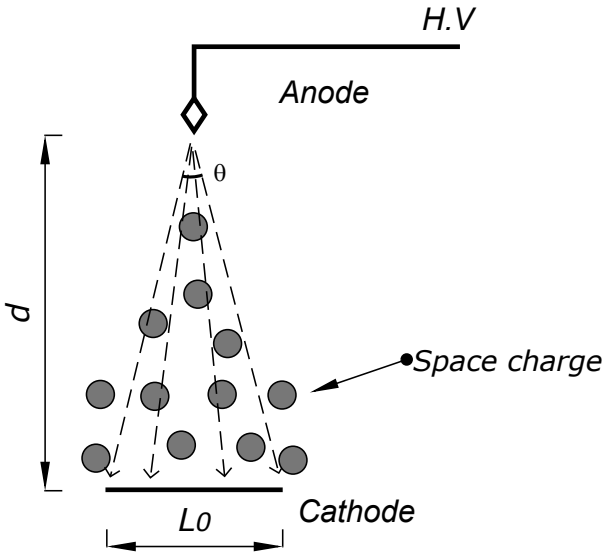

Figure 3.6: The non-uniform external electric field with the space charge effect

Chapter 4

Experiments of Ion Deflections

4.1 The Discharge Configurations

The discharge experimental setup consisting of six modules is shown in Figure 4.1. These modules are: (a) a DC power supply, (b) a high voltage circuit, (c) a discharge tube, (d) a pressure sensor, (e) a vacuum pump, and (f) an output signal processing circuit.

4.1.1 High Voltage Circuit and Load Resistor Technique

- High voltage circuit

  The high voltage circuit is a battery-powered device that provides sufficiently high breakdown voltage for gas discharges in argon. The schematic diagram of the circuit is shown in Figure 4.2. Devices ① and ② are operational amplifiers (LF 257) working as a Sinusoidal wave generator with a regulated peak-to-peak output voltage of 1.4 V. This signal is subsequently amplified by ③, which is another operational amplifier(LF 257). Output of this stage is further amplified by using a transformer ④ (MET -17) up to approximately 110 V. Subsequently, the AC voltage is rectified to a DC voltage ranging from 550 -750 V by the voltage multiplier ⑤ (PVM 302P12). ⑥ and ⑦ are two operational transconductance amplifiers in the chip LM 13700. They are used in the feedback loop to stabilize the output voltage. This circuit provides an adjustable output voltage that is sufficient for argon discharges in our low pressure discharge system.

- Load Resistor

  The load resistor is used to ensure that the discharge occurs in the desirable regime by limiting the discharge current. Ideally, a load line intersects the discharge I-V curve at only one point, and this results in a stable operating point of the gas discharge. In Figure 4.3, the load line with $R = 500\ k\Omega$ and $V = 450\ V$ would be an example. In the other extreme, a load line can intersect the I-V curve at multiple points to yield

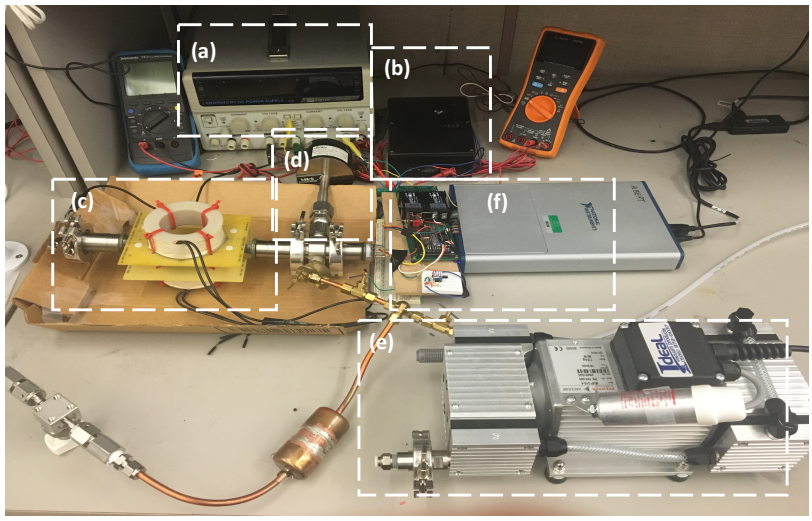

Figure 4.1: Experimental setup of ions deflection

multiple operating points, which can be both stable and unstable operating points. The load line with 500 $k\Omega$ and $V = 300\ V$ would be an example. The corona discharge regime is a highly unstable discharge regime with a negative resistance, which the current increases corresponding to the decrease of the discharge voltage. When using a larger resistance and a higher discharge voltage, the load line intersects with the I-V curve at only one point located in the corona discharge regime. For example, when a load line has a resistance of 5,000 $k\Omega$ and the discharge voltage is 700 V, the gas discharge has one operating point in the corona discharge regime. Therefore, using a current source with an almost infinite output resistor is advantageous, as it produces a single operation point on the I-V curve.

Hence, by carefully adjusting the current level and applying sufficient voltage, it is straightforward to operate in the corona discharge regime.

4.1.2 Output Signal Processing Module

As shown in Figure 4.4, this module is divided into a current-to-voltage conversion circuit and a data acquisition system (DAQ). The DAQ system consists of a multiplexer (MUX), a programmable-gain amplifier (PGA) and an analog/ digital converter (ADC). The current signals from the discharge device are converted into the voltage signals, and voltage outputs are connected to different channels of the DAQ for further analysis. For the I-V conversion circuit, an input current signal I_0 corresponds to an relative output voltage signal $V_0 = I_0 \times R_f$. Considering the input current has a range from 0 μA to 32 μA, and the full scale of voltage measurement for the DAQ is $\pm$ 10 V, we have chosen 220 $k\Omega$ for the value of R_f. Thus, the voltage measurement range of the DAQ is suitable for our output voltage signals. This DAQ (NI- USB 6343) has a full sampling rate of 500 kS/s and 16-bit A/D or

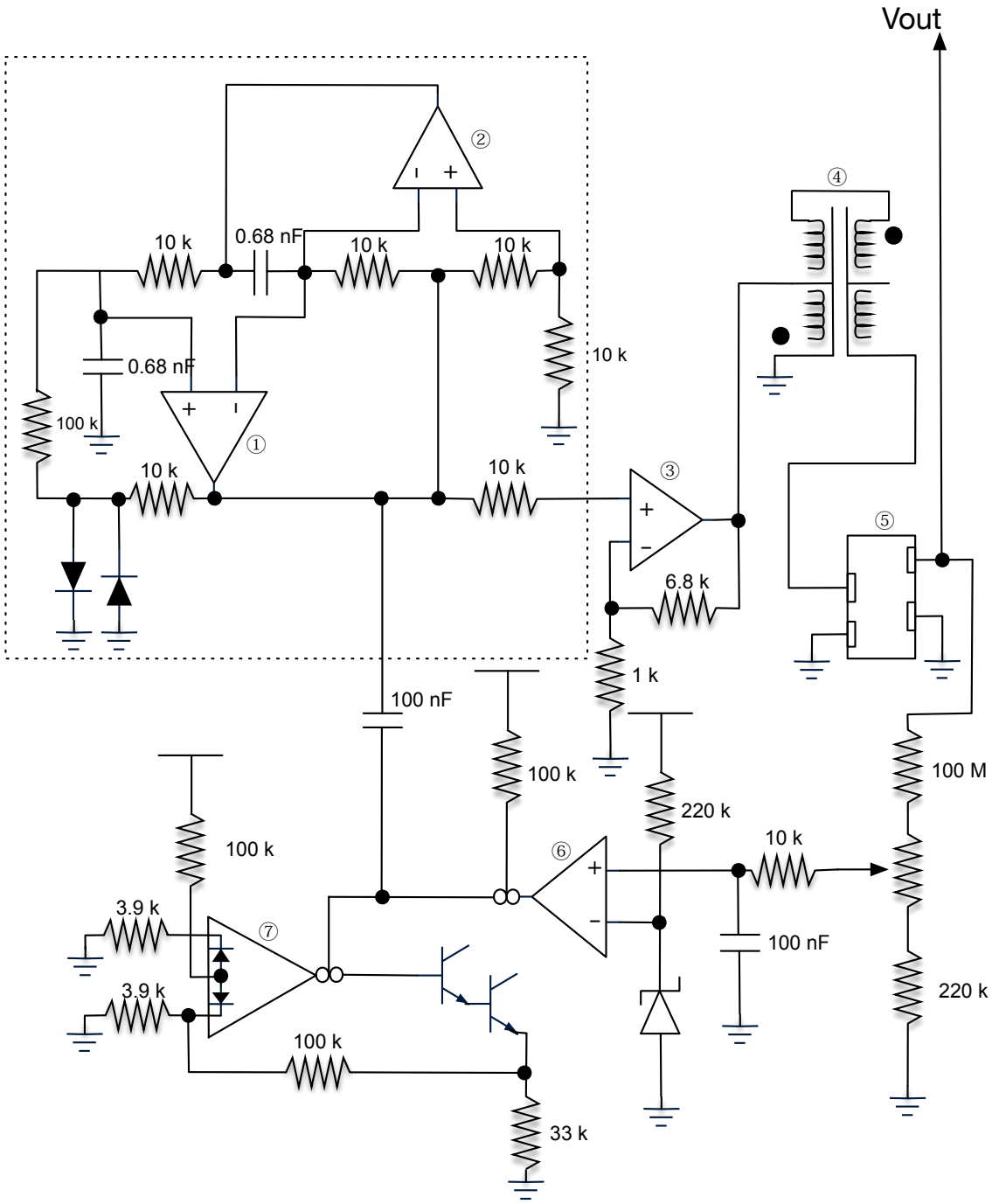

Figure 4.2: Schematic diagram of the high voltage circuit.

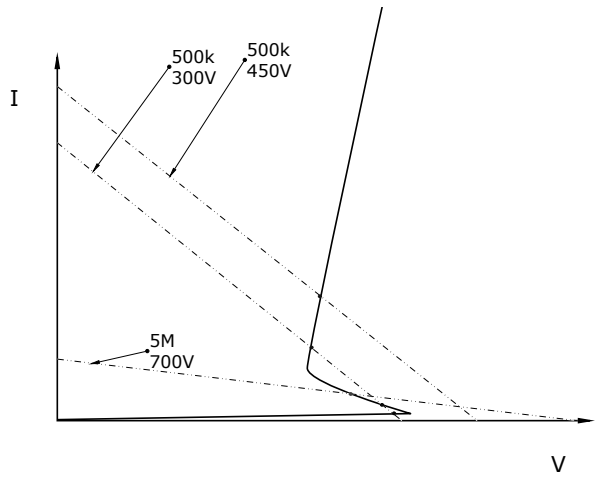

Figure 4.3: Plot of typical gas discharge I-V showing various resistor loading lines.

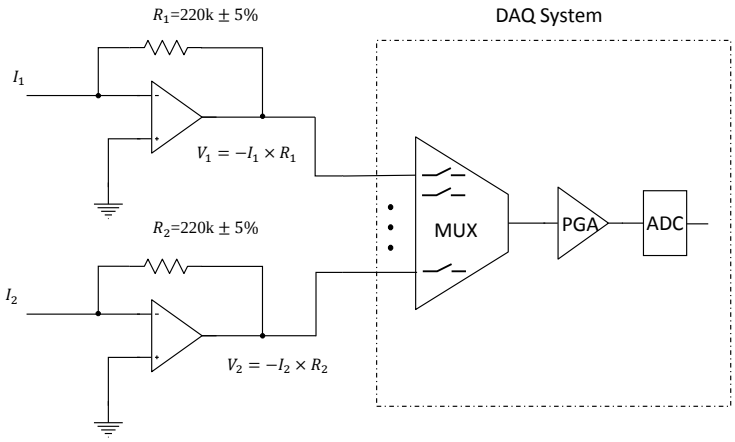

Figure 4.4: Current to voltage conversion circuit and the DAQ

D/A resolution. The least significant bit for the device can be found from:

$$\frac{20}{2^{16}} = 0.3\ mV \tag{4.1}$$

$$I = \frac{V}{R} = \frac{0.3\ mV}{220\ k\Omega} = 0.0014\ \mu A \tag{4.2}$$

A user interface has been built using Labview to obtain a real-time waveform monitoring.

4.1.3 The Vacuum Chamber

A glass-to-metal feedthrough chamber is used in ion deflection experiments. The plastic chamber was abandoned because it adsorbs contamination from the air and releases it into the chamber, which disturbs the low pressure environment. The contamination can be removed with a strong chemical solvent, though the plastic chamber may not tolerate it. In contrast, a metal chamber will absorb less contamination and be able to withstand the use of a strong chemical solvent. Metal materials typically have high magnetic permeability, which can affect the magnitude of the magnetic field. As a result, a glass-to-metal with Kovar feedthrough chamber is desirable for the following characteristics: (1) The external field can be applied at the glass section, where it has less influence on the magnetic field; (2) The glass section insulates high voltage from other metal parts avoiding short circuits. (3) A brass end plate sealing one end of the chamber can also provide the electrical connection to high voltage circuit. National pipe thread and compression fitting connectors are used to connect the chamber with additional vacuum parts, such as the vacuum pump and the pressure control sensor.

Outgassing and leaking are two critical variables that can influence the performance of the vacuum system. Lowering the outgassing level can provide a lower operating pressure and higher concentration of the discharge gas. In addition, reducing the leakage rate can ensure a stable gaseous environment and improve the repeatability of experiments.

Outgassing Phenomenon

The outgassing process is the release of air dissolved in the chamber walls. It leads to an increase of the gas pressure in the discharge chamber. Thus, it becomes a challenge of maintaining a clean argon environment. To minimize outgassing, the discharge chamber was disassembled, cleaned in acetone, rinsed by isopropyl alcohol and baked in an oven to remove most contaminations. Measurements of outgassing levels were carried out after the cleaning process. The following procedures were followed:

1. The discharge chamber was exposed to the air for 2 hours and pumped down by a dry vacuum pump to its lowest pressure capability of the pump for approximately 30 minutes.

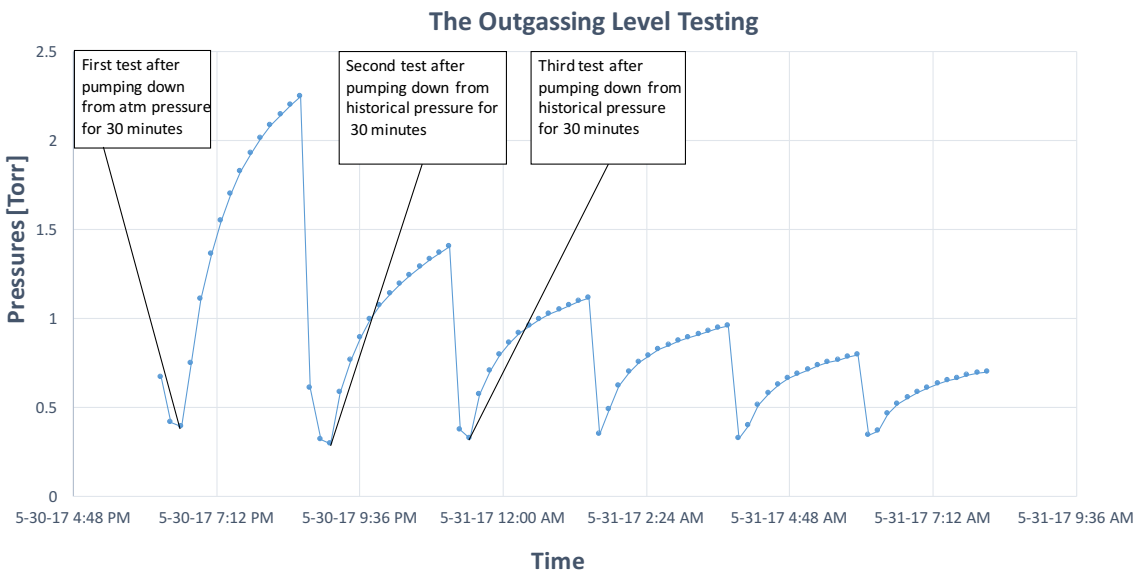

Figure 4.5: The outgassing level testing

2. The vacuum pump was powered off and changes of pressure signal were recorded by the DAQ for 2 hours to estimate outgassing levels and leakage rates.

3. The vacuum pump was powered on for another 30 minutes' vacuumizing process, and powered off for another 2 hours of the pressure recording.

4. Step 3 was repeated 4 times.

The experimental results are plotted in Figure 4.5. The level of outgassing for the first experiment was 2.2 torr, the second outgassing level was 1.4 torr and the third outgassing level was 1.1 torr. The level of outgassing inside the discharge chamber decreases with pumping time, which is probably due to contamination absorbed by the glass chamber wall, and then released during vacuumizing. Gradually, the vacuum pump removed the contamination. The absorbing process was slow at room temperature while the degassing by the vacuum pump was rapid. As a result, the outgassing level became lower and lower even though a certain amount of contamination residue existed in the chamber, because of the thermodynamic equilibrium. Since a clean argon environment is desirable for deflection experiments, we pumped down the chamber until we reached the smallest outgassing level and flushed this chamber with argon multiple times to obtain a high purity argon chamber. Since outgassing is a thermodynamic process, decreasing environmental temperatures can influence the thermal equilibrium, and thus, the outgassing level.

Leakage Rate

Leakage testing was conducted to find out the performance of the vacuum system and potential bad connections. Most of the leakage was found from connections between com-

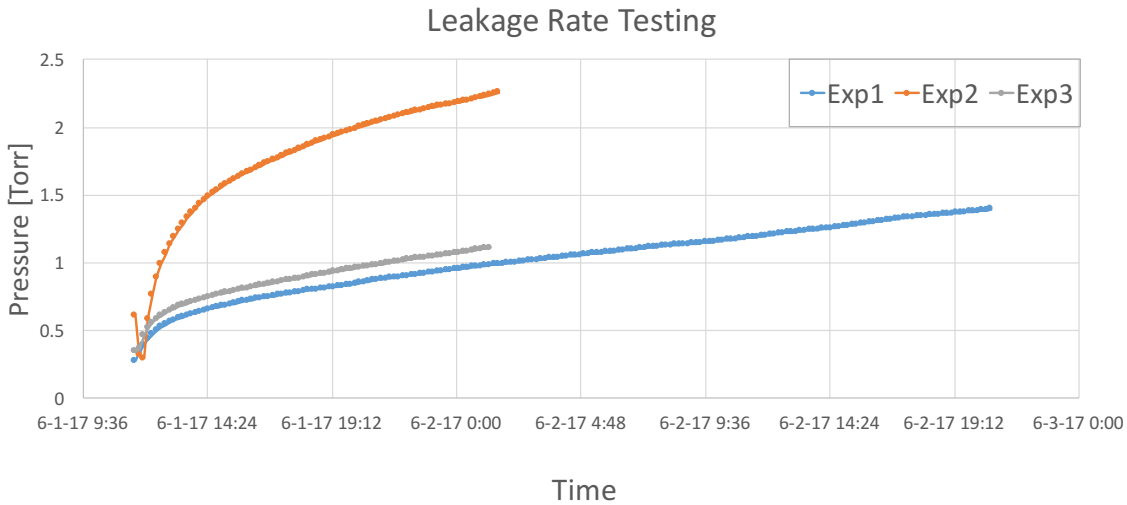

Figure 4.6: Leakage testing at different outgassing levels

ponents. To enhance the performance of connectors, Teflon tapes were used to wrap threads of connectors. Following that, the pressure changes were recorded over time to estimate the leakage rate (Figure 4.6). Leakage rates can only be estimated after the completion of the outgassing since both processes contribute to increments in the pressure level. Outgassing is an fast process compared to leaking, once a thermal equilibrium is achieved, the outgassing level is determined and only the leakage contributes to the increase of the pressure level.

According to Figure 4.6, the outgassing appeared in the first 2 to 4 hours while leaking did not stop at all. When the level of outgassing was greater, it lasted longer. The linear regions that had a slope value of 0.45 demonstrated a process with the pure leaking processes. As a result, the leakage rate of a well-prepared chamber was approximately 0.45 torr per day, which is sufficient for the following experiments.

4.1.4 Magnetic Coil

Two sets of FC-4838 magnetic coils were used to produce the magnetic field needed for the ion deflection. The coil of 1350 turns has a length of 25.4 mm and an inner radius of 25.4 mm. To characterize the magnetic field produced by these two coils, the vacuum chamber was placed between two aligned coils as shown in Figure 4.7. A pre-calibrated Hall sensor was placed at the midpoint between two coils inside the vacuum chamber, and it was approximately 12.7 mm from each coil. The two coils were connected in parallel and an ampere meter was used to measure the current in one coil. Figure 4.8 shows the characteristics of the aligned magnetic coils. The x axis is the current value measured by the ampere meter in mA, and the y axis is the corresponding magnetic field produced in mT. The maximum current applied in the experiments was 0.65 A, which produced an output of 15 mT. The relationship between the current and the output magnetic field is a

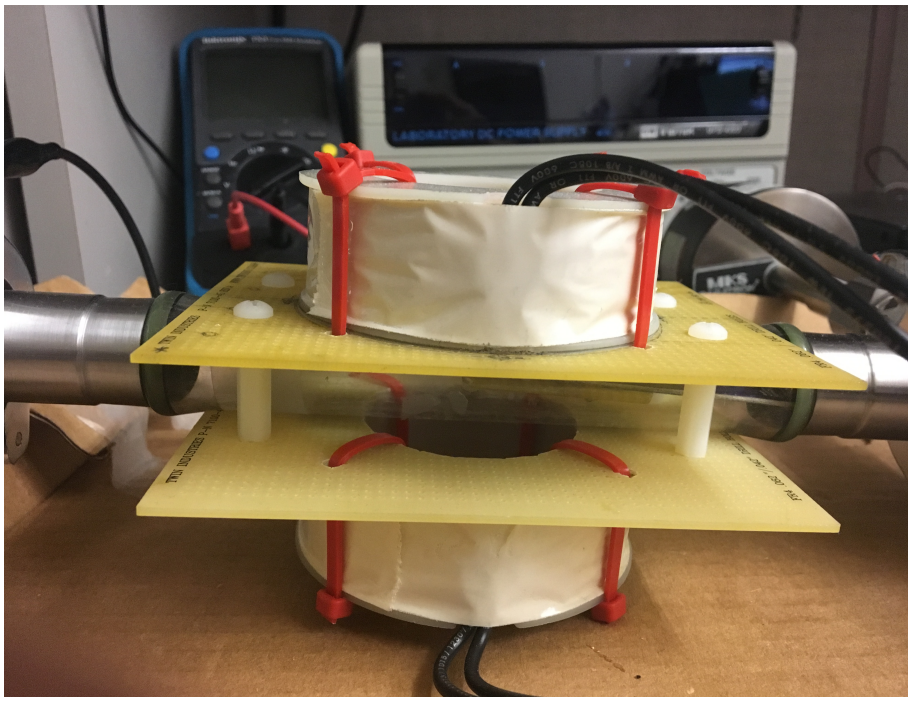

Figure 4.7: The two sets of coils were aligned for characterizing

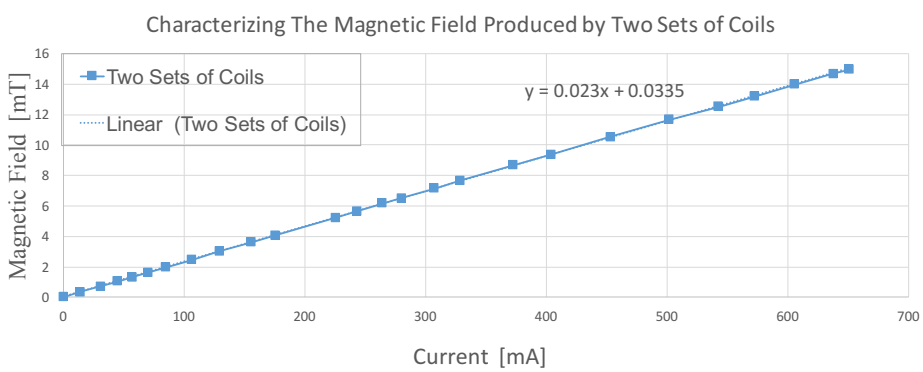

Figure 4.8: Characteristics of the magnetic field and currents

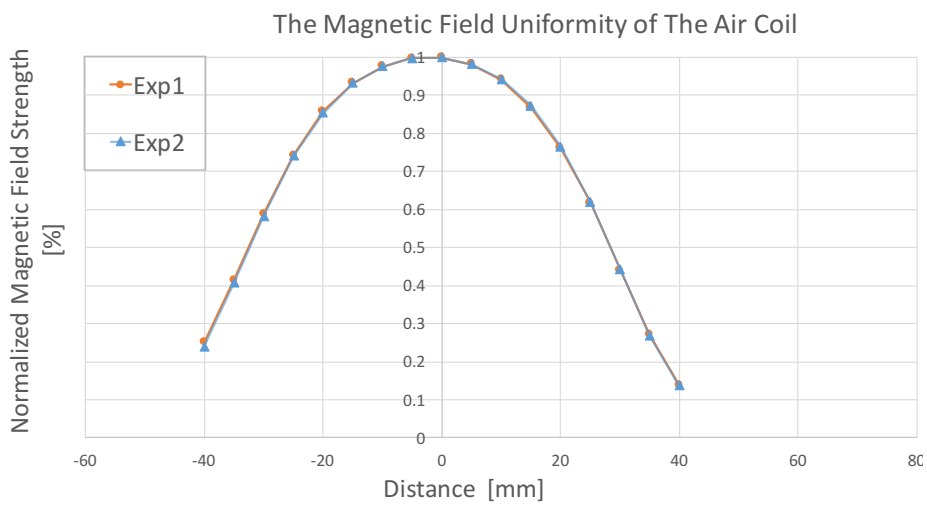

Figure 4.9: The magnetic field uniformity of the two sets of coils

straight line with a slope of 0.023. This also demonstrates the magnetic field produced by the two sets of coils is linear in the measured range.

In the later deflection experiments, the discharge device had a maximum discharge distance of 20 mm, and ideally this area should be located in a uniform magnetic field. We wanted to verify whether this coil pair could provide a uniform magnetic field, and also find out the experimental error introduced by the magnetic coil pair.

The midpoint was marked as $x = 0$ in the reference axis. The coils were located from $x = -25\ mm$ to $x = 25\ mm$, and the measurement of the magnetic field was started from $x = -40\ mm$ to $x = 40\ mm$. The results have been normalized and plotted in Figure 4.9. According to those data, the midpoint $x = 0$ has the greatest strength, and the magnetic field strength decayed with the distance from the midpoint. When $x = \pm 25\ mm$, at the edge of the coils, the difference between the magnetic field of the center point and the magnetic field of the edge is approximately 25%. This instrumental error would be a challenge of the reproducibility and accuracy of deflection experiments. Optimally, the discharge gap was designed to be in the range from $x = -13$ mm to $x = 13$ mm, where the maximum difference in the magnetic field strength is $\pm$ 11%. This area is also sufficient to accommodate the largest discharge gap we used in our deflection experiments, which was 20 mm.

.

4.2 Deflection Experiments

In order to find out the feasibility of ion beam gyroscopes, it is important to explore characteristics of ion deflections. The questions that need to be answered are whether ion deflections generate measurable output signal in our discharge tube and how do relevant variables affect the sensitivity of the deflection experiments.

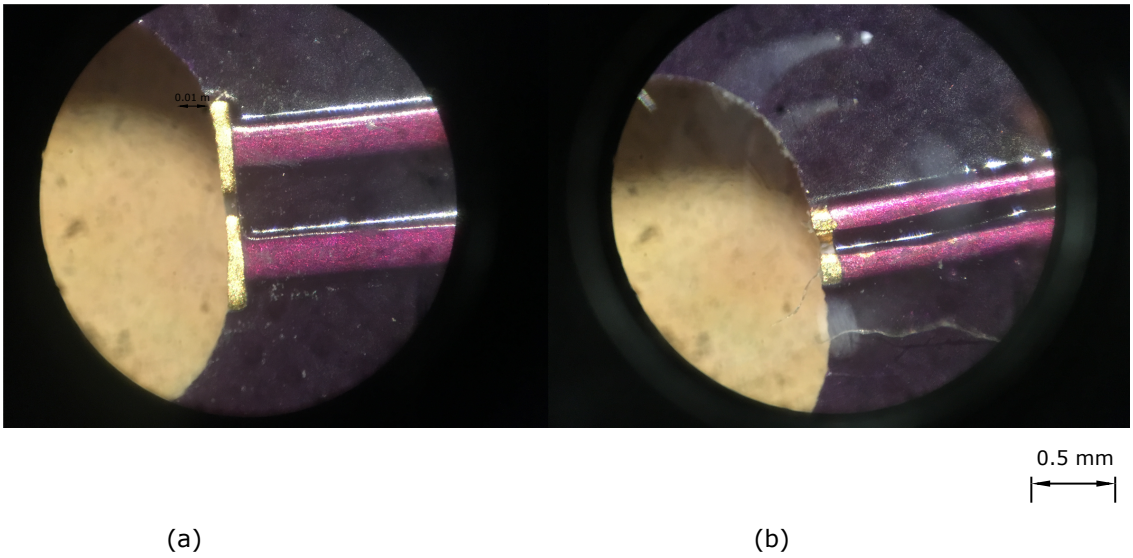

Figure 4.10: Photos of cathode layouts: (a) pin-plate and (b) pin-pin structure

4.2.1 Discharge Device Structures

Discharge devices we used in later deflection experiments can be classified into two categories by their cathode area: pin-pin structure and pin-plate structure. Figure 4.10 shows the cathode layouts for two structures.

- Pin-pin Structure

  Figure 4.10 (b) is the cathode layout of the pin-pin structure. The single anode and dual cathodes are made of copper traces with a width of 0.15 mm and a thickness of 0.035 mm on a printed circuit board (PCB). The metal traces are covered with solder-mask, except for the tip section of the copper traces that are exposed as cathodes. The clearance between two cathodes is 0.15 mm.

- Pin-plate Structure

  Figure 4.10 (a) shows the pin-plate structure. The exposed metal areas, which are recognized as cathodes, and they have a width of 0.6 mm (which is 4 times that of the pin-pin structure). And the copper traces connected to cathodes have a width of 0.30 mm (2 times of the pin-pin structure) and a thickness of 0.035 mm. And the clearance of two cathodes stays as 0.15 mm.

4.2.2 Ion Deflections vs. Magnetic Field

Previous work [43] has shown that electrons can be deflected by a small magnetic field. In contrast, since an ion has a charge-to-mass ratio smaller than an electron's, the magnetic field needed to deflect ions is at least four orders of magnitude larger than that of electrons. To determine the minimum magnetic field needed for an detectable ion deflection, the relationship between the ion deflection and the magnetic field must be examined. Experiments were conducted with both the pin-pin structure device (Device 1) and the pin-plate structure (Device 2).

Device 1 is a pin-pin discharge device with a discharge distance of 2.5 mm, while Device 2 has a pin-plate structure with a discharge distance of 20.3 mm. Ions drift from the anode to cathodes causing two current signals on cathodes. The current signals of Cathode 1 and Cathode 2 are denoted by I_1 and I_2 respectively. With the effect of various magnetic field strengths, I_1 and I_2 change accordingly. The current change on Cathode 1 is defined as ΔI_1. Similarly, ΔI_2 is the current difference on Cathode 2. Since the total discharge current of this experiment was controlled by a current source with an output value, so $|\Delta I_1| = |\Delta I_2|$. The percentage of ion deflection $Def(\%)$ is the difference between deflected ions on Cathode 1 and that on Cathode 2 over total amount of ions.

$$Def(\%) = \frac{\Delta I_1 - \Delta I_2}{I_1 + I_2} \cdot 100\% \tag{4.3}$$

Further, the differential current $Diff(\mu A)$ is the current subtraction of the current difference on Cathode 1 and that on Cathode 2, which is calculated as:

$$Diff(\mu A) = \Delta I_1 - \Delta I_2 \tag{4.4}$$

And sensitivity Sen of the ion deflection experiment can be defined as

$$Sen = \frac{Diff(\mu A)}{B} \tag{4.5}$$

Where B is the magnetic field strength. Results are shown in Figure 4.11 for Device 1 and in Figure 4.12 for Device 2. Both $Def(\%)$ and $Diff(\mu A)$ are linearly proportional to the magnetic field. Previous works, such as mass spectrometers, have shown that ions can be deflected in a high vacuum environment. However, our experiments demonstrate that even at a much lower vacuum, and with smaller drifting region, a measurable signal of ion deflection can be attained. For example, a magnetic field of 15 mT, which is 300 times of the earth's magnetic field, could produce a differential current of 0.6 μA when the total discharge current was 26 μA. Consequently, we can cautiously conclude that the ion beam gyroscope is feasible and it has a small interference from the earth's magnetic field.

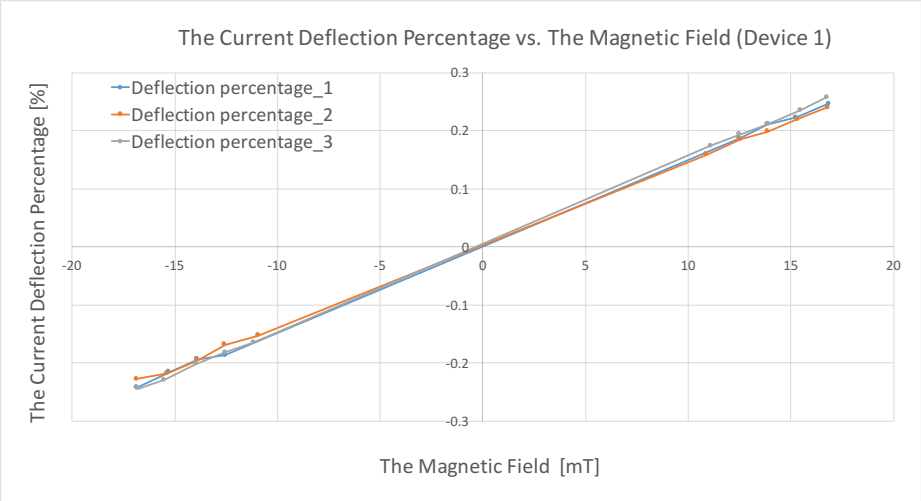

(a) Deflection percentage vs. magnetic field (Device 1)

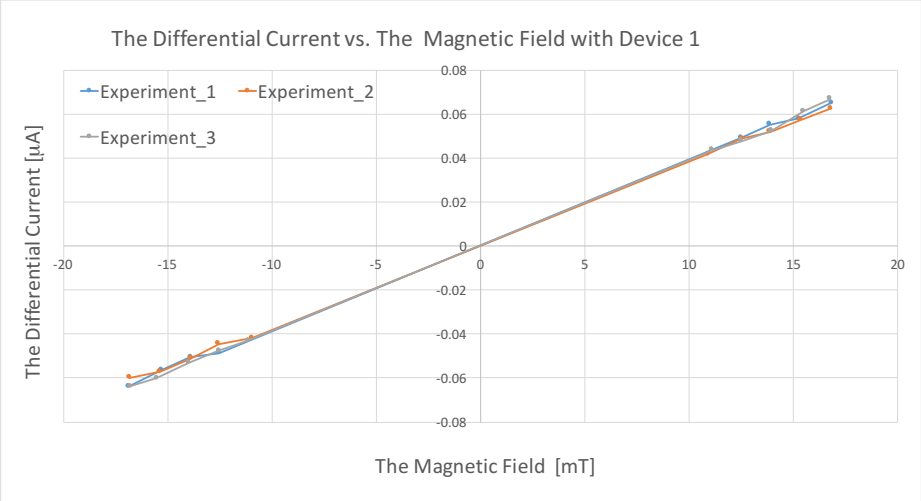

(b) Differential current vs.magnetic field (Device 1)

Figure 4.11: Influences of the magnetic field on ion deflections (Device 1)

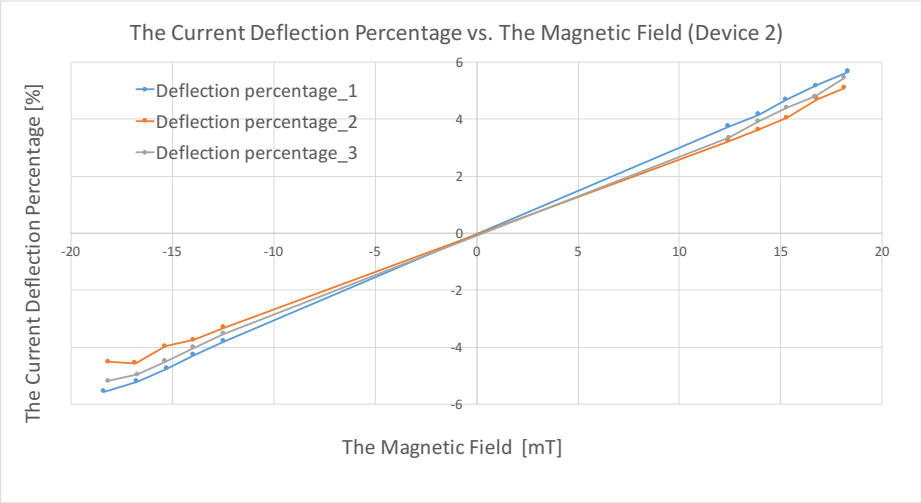

(a) Deflection percentage vs. magnetic field (Device 2)

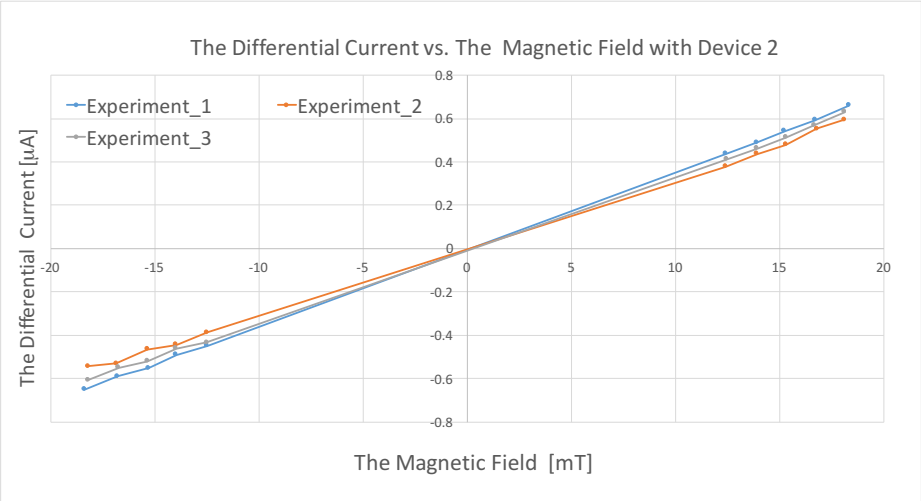

(b) Differential current vs. magnetic Field (Device 2)

Figure 4.12: Influences of the magnetic field on ion deflections (Device 2)

4.2.3 Ion Deflections vs. Discharge Distance

Discharge distance is complicated on the impact of ion deflections. On one hand, increasing the discharge distance d results in a longer drifting region. On the other hand, larger breakdown and discharge voltages are required for a larger d, according to Paschen's law. To explore how the drifting field is affected by d, we derived a formula based on Paschen's equation [50].

$$V_{bd} = \frac{C_1 d}{ln(C_2 d) - C_3} \tag{4.6}$$

where V_{bd} is the breakdown voltage and C_1, C_2, C_3 are constants governed by the operating pressure and the gas type. The breakdown electric field is described as

$$E_{bd} = \frac{V_{bd}}{d} = \frac{C_1}{ln(C_2 d) - C_3} \tag{4.7}$$

For our experimental condition, the constant $C_2 = 56.50\ cm^{-1}$ [50], therefore $C_2 d > 1$ and $ln(C_2 d) > 0$. This implies that increasing the discharge distance d leads to a smaller breakdown field.

Nevertheless, the breakdown field is different from the drifting field. The breakdown voltage drops to a lower value, known as the discharge voltage, immediately after gas breakdown. Due to the internal phenomena, like self-building electric field, the breakdown voltage is generally higher than the discharge voltage. The relationship between breakdown voltage and discharge voltage remains poorly understood. My hypothesis is that the breakdown voltage and the discharge voltage are positively correlated. If it is true, increasing the discharge distance will also result in a smaller drifting field. To study the impact of discharge distance on discharge voltage and drifting field, experiments were conducted, and results are shown in Figure 4.13 .

According to Figure 4.13 (a), the discharge voltage increases slightly with the discharge distance, indicating that the gas discharge operates at the right side of the valley of Paschen's curve. The results from Figure 4.13 (b) suggest that the drifting field decreases with discharge distance. On the basis of the results, my hypothesis is that a longer discharge distance leads to a smaller drifting field. The acceleration rate of the drift velocity is smaller, thus, it takes longer for ions to arrive at cathodes along the x axis, and the ion displacement in the y axis is larger correspondingly. To confirm this theoretical speculation, extensive experiments, and their relationship are shown in Figure 4.14. As the discharge distance increases, the percentage of ion deflection increases monotonically. In Figure 4.14, solid lines represent the results for pin-plate discharge devices, while the dotted lines correspond to pin-pin discharge devices. According to the theoretical model discussed in the previous chapter, doubling the discharge distance would result in four times of the deflection displacement in the y axis. If the deflection displacement is proportional to the percentage of ion deflections, the current deflection percentage should also be four times when the dis-

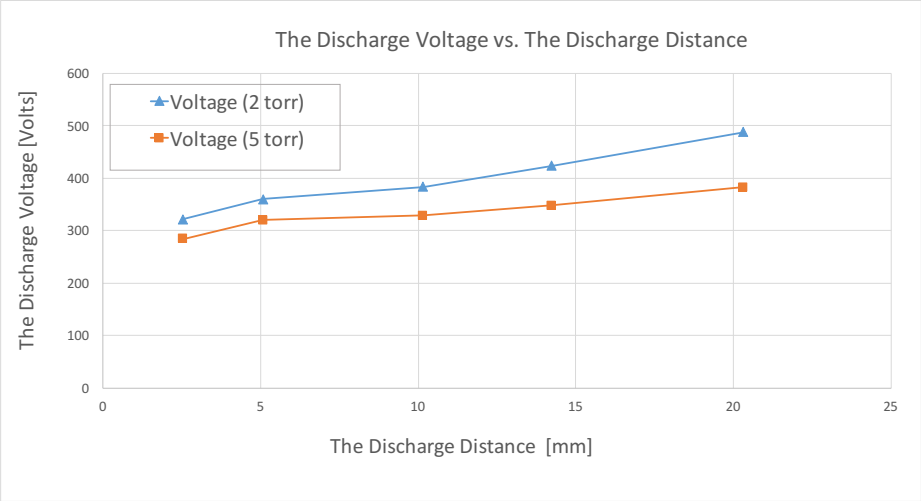

(a) The relationship between discharge Voltages and discharge distances

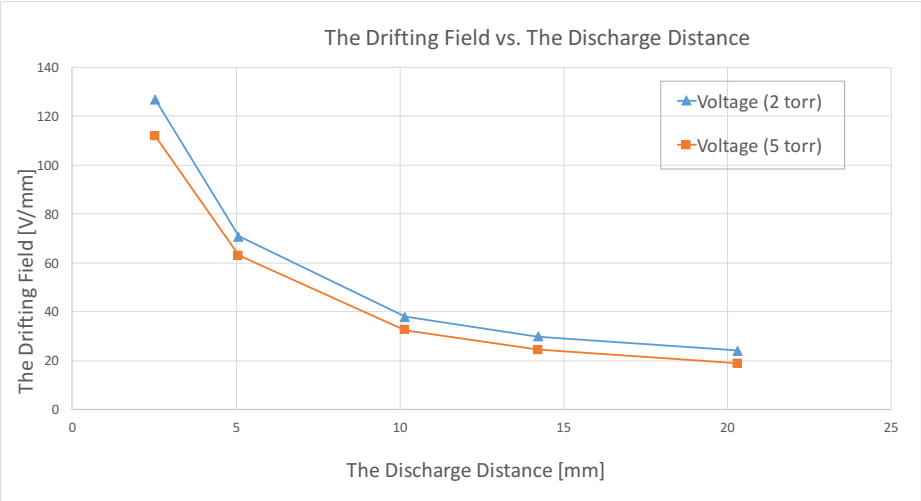

(b) The relationship between drifting fields and discharge distances

Figure 4.13: Influences of discharge distances on both discharge voltages and ions drifting fields

charge distance doubles. Nevertheless, the experimental data are slightly smaller than one time increment of ion deflection percentage when the discharge distance is doubled, which does not match well with the theoretical model and the above speculation. And this tendency has been observed in both pin-pin devices and pin-plate devices. This phenomenon can be qualitatively interpreted as the drifting field declining when the discharge distance becomes greater, and a smaller acceleration rate and longer travel time in the x direction is favored for a longer deflected displacement in the y direction. To conclude, experimental results are consistent with our theoretical speculation that the drifting field declines when discharge distance becomes greater, which causes a larger deflection displacement in the y

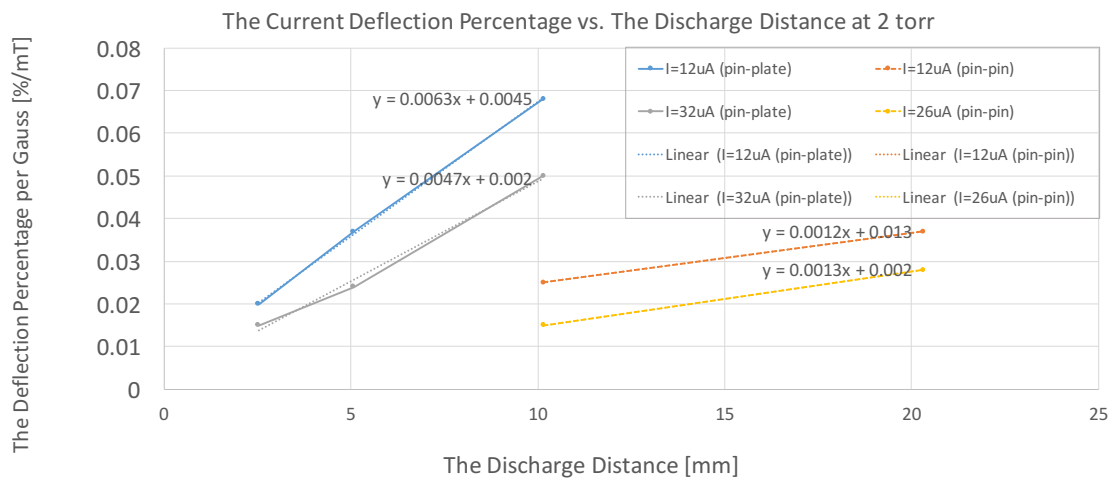

Figure 4.14: Relationship between ion deflection and discharge distances at 2 torr with both pin-pin device and pin-plate device

direction. The discharge distance has a more significant impact on pin-plate devices than pin-pin devices.

4.2.4 Ion Deflection vs. Discharge Current

The discharge current is thought to be an important variable that affects both the durability of discharge devices and the sensitivity of the ion deflection experiments. Gas discharges are desired to be confined in the corona discharge regime, which restricts the value of the discharge current to be from few μA to a few mA. Besides that, there are further constraints on the discharge current.

1. Lifetime of cathodes

   Ions drift to cathodes will bombard them and sputter contamination on them. As the discharge current increases, larger amounts of ions severely collide and erode the cathodes, which significantly reduces the lifetime and reliability of devices. Figure 4.15 compares the device before gas discharge with the device after 80 hours of discharge.

2. Divergence of ion beams

   Because of the repulsive force between ions, a larger discharge current will lead to a more divergent ion beam. This in turn has a negative effect on the performance of the deflection experiment. Thus, small current values are of advantage for better sensitivity.

3. Signal-to-Noise Ratio

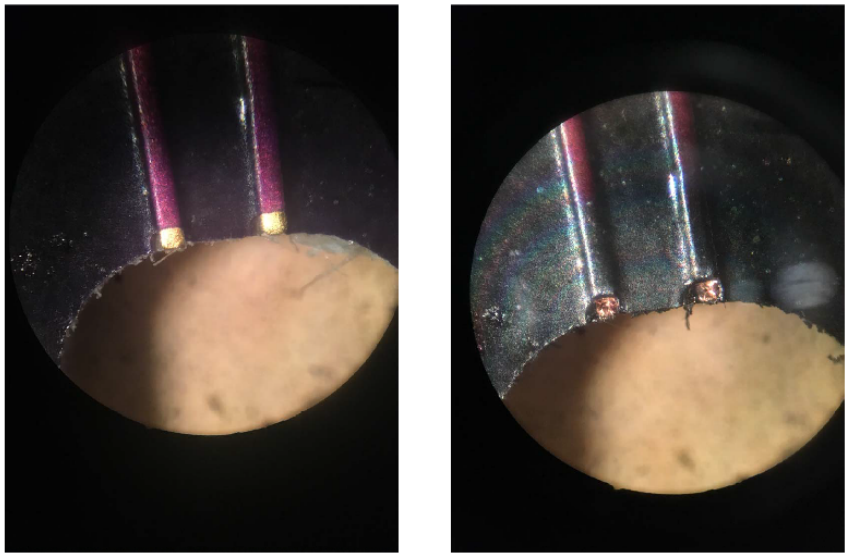

(a) (b)

Figure 4.15: Influence of ion bombardments on cathodes: (a) before the gas discharge; and (b) after 80 hours of discharge

In contrast, if a discharge current is too small, the current signals collected by each cathode are small for the signal processing modules. Since the instrumental noise and external interference level stay as constant, the signal-to-noise ratio is smaller compared to that of a large discharge current.

4. Signal Oscillations

   Previous work has recorded the appearance of current oscillations in DC positive corona gas discharges [51, 52, 53]. The amplitude of the signal oscillation varies with different discharge currents. The oscillation affects the observation of deflection experiments since it sets obstacles for measuring the output signal in the constrained scale. Thus, a certain range of current should be avoided.

To explore how the total discharge current affects the ion deflection, experiments were carried out with both pin-pin and pin-plate discharge devices. Figure 4.16 shows the results of experiments at 2 torr and Figure 4.17 shows that at 5 torr. The total discharge current provided by the current source increased from 12 μA to 32 μA. From Figure 4.16 (a) and Figure 4.17 (a), we can conclude that the deflection percentage of ions tends to decline with increases in the discharge current. The dotted lines are results of the device with a discharge distance of 5.1 mm and the solid lines are results of the device with a discharge distance of 10.2 mm. According to the results, the percentage of the ion deflection decreases with the

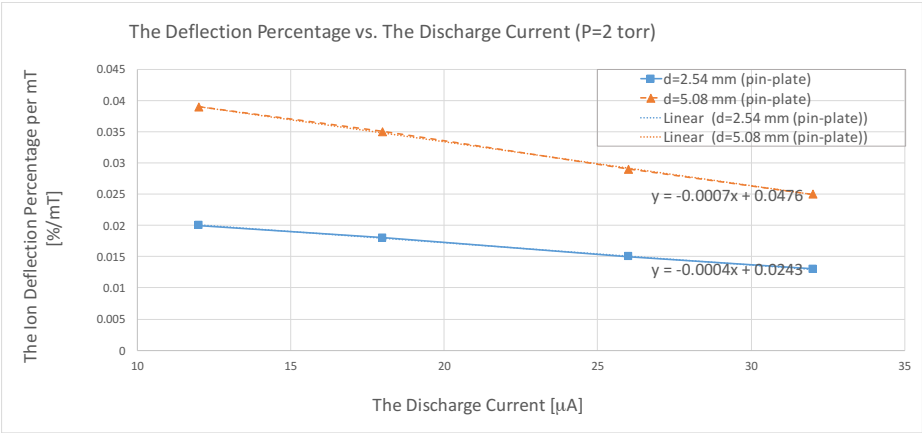

(a) Discharge percentage vs. discharge current at 2 torr

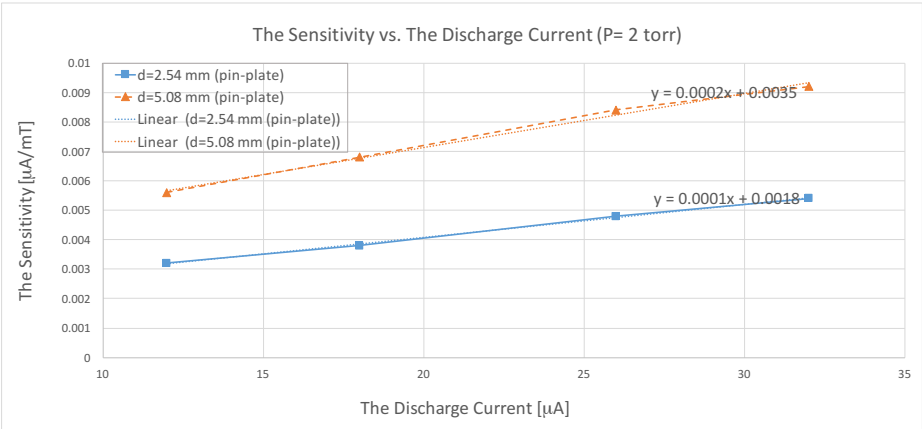

(b) Sensitivities vs. discharge current at 2 torr

Figure 4.16: Ion deflections vs. discharge current at 2 torr

discharge current while the sensitivity increases with the discharge current. Meanwhile, the dot lines have slope values twice those of the corresponding solid lines, which implies that the discharge current has a heavier impact on discharge devices with larger distances.

The ion beam produced by gas discharges has a Gaussian distribution in the drifting field, a convergent ion beam is thought to have a larger deflection percentage compared to that of a divergent ion beam for the same displacement in the y axis. Different discharge currents are normalized to 1, and the distribution with a larger discharge current is more divergent. In Figure 4.18, the solid lines are the distributions of the convergent ion beam and the dotted lines show the distributions of the divergent ion beam with the same discharge current. For each ion beam, we plot its original profile and the profile with a displacement of 2 mm along the reference axis emulating the influence of the magnetic field deflection. Shadow areas are the differential ion percentage produced by the displacements. The convergent beam has a larger shadow area, indicating that the ion deflection

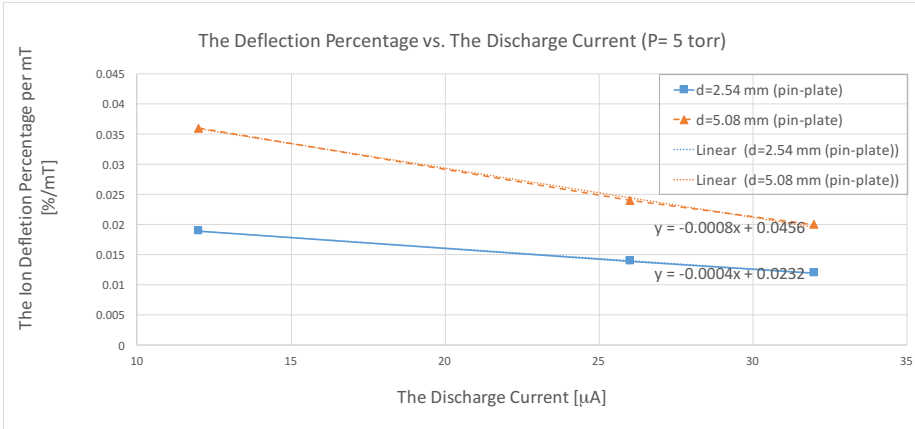

(a) Discharge percentage vs. discharge current at 5 torr

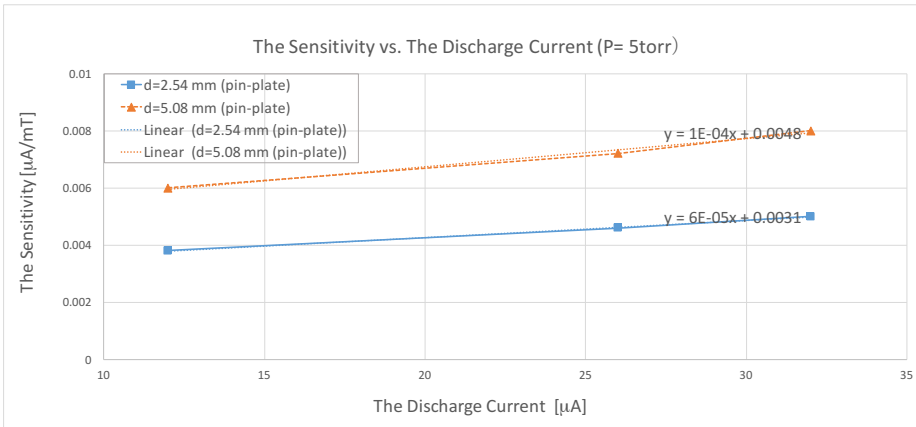

(b) Sensitivities vs. discharge current at 5 torr

Figure 4.17: Ion deflections vs. discharge current at 5 torr

percentage decreases with larger currents. This matches well with the experimental results. On the other hand, the amount of ions deflected by the magnetic field increases with the discharge current even though the percentage of deflected ions declines. To conclude, experimental data demonstrates that the differential current per unit magnetic field, which is the sensitivity value of the sensor, increases with the discharge current.

4.2.5 Ion Deflections vs. Pressure

Operating pressure of the deflection experiment were confined from 1 to 10 torr for two reasons: (a) the high voltage circuit can only supply a limited high voltage up to 750 V, which determines the maximum operating pressure; (2) the outgassing level of the discharge chamber stays at 0.5 torr, which restricts the minimum operating pressure. On one hand, pressure is an independent variable that affects the drifting velocity and collision frequency of the ion beam. On the other hand, pressure has an influence on the discharge voltage, and

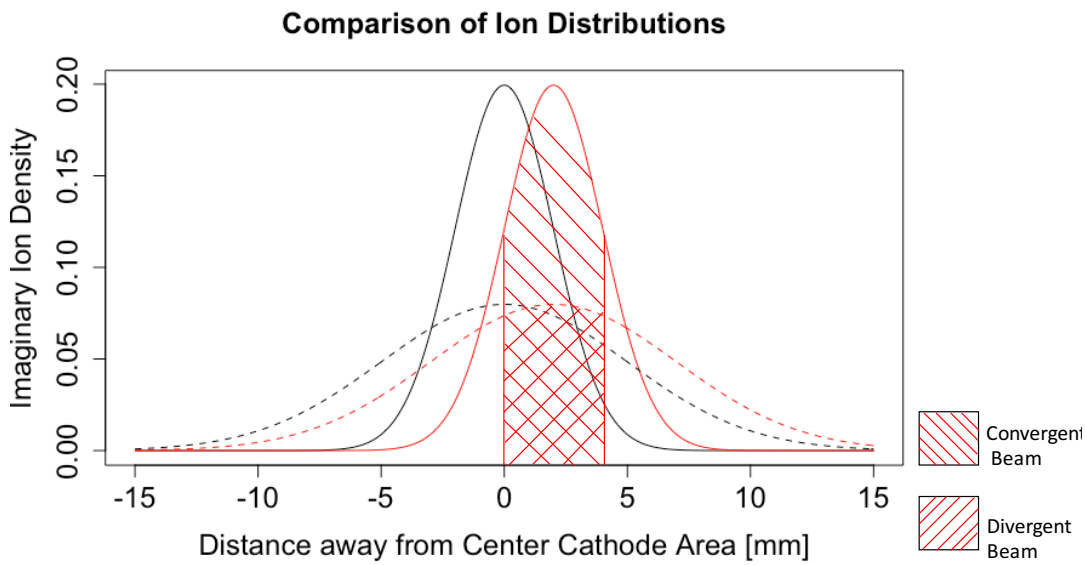

Figure 4.18: Comparison between ion displacement for divergent beam and converged beam

their relationship can be described as a non-monotonous function. According to Paschen's law, the breakdown voltage drops with the increments of pressure in the left side of Paschen's curve and increases with pressure in the right side of Paschen's curve for a given discharge distance.

The value of Pd_{valley} for argon gas is approximately 4 $torr \cdot mm$ [54], while the operating range for our experiments was from (2 - 200) $torr \cdot mm$. Considering that the gas filling the discharge chamber is the mixture of a high percentage of argon gas, a lower percentage of air and a small percentage of contamination. This leads to a larger value for Pd_{valley} compared to the reference value of Paschen's curve for a pure argon environment. Therefore, the relationship of pressure with discharge voltages has a bifurcated profile with varied pressure values. Explorations of the relationship have been done experimentally and the results are shown in Figure 4.19. The dotted line shows the relationship between the discharge voltage and pressure for a device with a discharge distance of 14.2 mm at 12 μA, while the solid line shows that for the device with d = 5.1 mm at 12 μA. The demarcation points are approximately 3 torr for the d = 14.2 mm device and 4 torr for the d = 5.1 mm device. It implies that these sets of ion deflection experiments were operating on both sides of Paschen's curve, which matches with our theoretical analysis.

Pressure plays an important role in affecting the sensitivity of ion deflection experiments. Thus, the exploration of the relationship of differential current and the pressures is needed to optimize experimental setup. Their correlations are shown in Figure 4.20. According to the results, both the deflection percentage and the sensitivity decline with the increasing of pressure. The explanation for this phenomenon is that increasing the pressure leads to

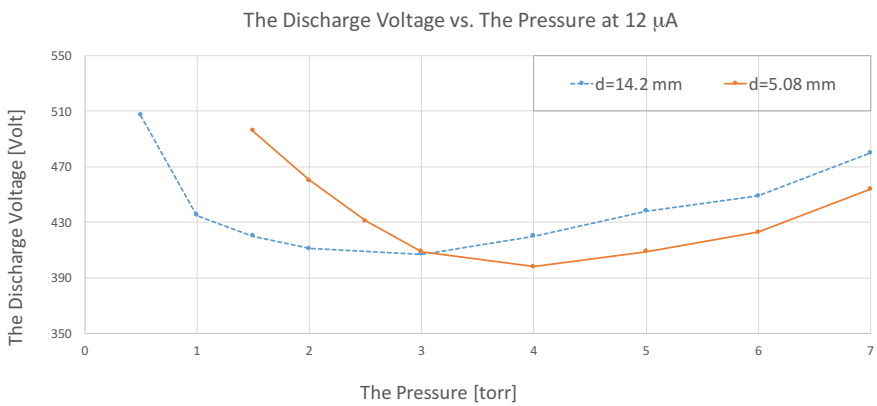

Figure 4.19: Discharge voltage with varied pressures at 12 μA

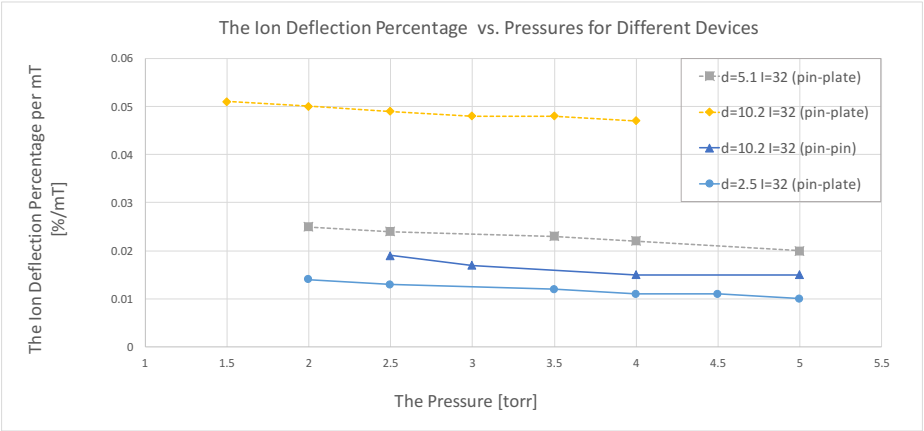

(a) Characteristic of ion deflection percentage and pressures

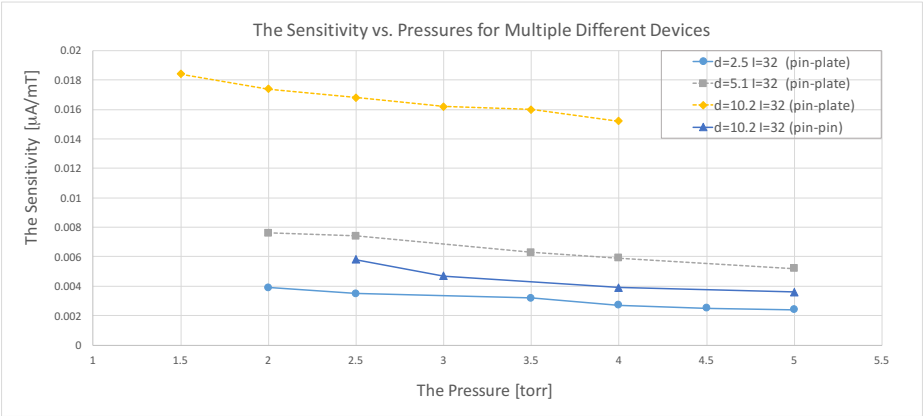

(b) Characteristic of sensitivities and pressures

Figure 4.20: Ion deflections with pressure at various distances and discharge currents

more collision and scattering of ions, which in turn causes a larger ion beam divergence.

Experiments demonstrate that the influence of pressure on sensitivities is not as significant as other relevant variables.

4.3 Discussion

4.3.1 Conclusion of Experiments

Experiments were conducted to explore the relationships between ion deflections and relevant variables. Conclusions can be drawn from the experimental data:

1. The sensitivity of ion deflections is linearly proportional to the discharge distance. This is due to the fact that a longer discharge distance leads to a smaller drifting field. Therefore, both a smaller drifting field and a larger distance contribute to a longer travel time for an ion and larger displacement along the y axis. Still, a trade-off is required to optimize the size of the sensor while maintaining a good sensitivity.

2. When discharge current increases, the percentage of ion deflection decreases with increases in the differential current. Thus, the sensitivity of deflection experiments increases with the total discharge current, and a larger current leads to a larger signal-to-noise ratio, which is advantageous in signal processing. However, a larger current may affect the lifetime of the electrodes, which in turn has a negative effect on the repeatability of deflection experiments and on the durability of discharge devices. Therefore, a trade-off is needed between the electrode lifetime and the resolution.

3. Sensitivity has a weakly inverse correlation with the pressure. High pressure brings in more frequent collisions, diverging the ion beam and reducing the drift velocity of the corresponding beam. It slightly reduces the differential current and the sensitivity.

4. A geometric structure also affects the sensitivity values. A pin-plate device has a larger sensitivity compared to a pin-pin device.

The theoretical formula (3.27) implies the displacement of the ion beam along the y axis is proportional to the magnetic field. Meanwhile, our experimental results prove that the differential current and the percentage of the ion deflection are proportional to the magnetic field. The displacement along the y axis can be concluded from the formula (3.27) that,

$$y \propto B$$

According to Figure 4.11, we can also deduce that,

$$Def(\%) \propto B$$

and

$$Diff(\mu A) \propto B$$

Therefore, we can speculate that both the ion deflection and the differential current are proportional to the ion displacement in the y axis,

$$Def(\%) \propto y$$

and

$$Diff(\mu A) \propto y$$

Since both $Def(\%)$ and $Diff(\mu A)$ are proportional to the displacement along the y axis, the theoretical model is of great importance in figuring out relevant variables and their impacts on the magnitude of the ion deflection. We need to notice here that due to our simplification assumption, some variables are not included in our model, such as area of cathodes, total discharge current, which may also influence the ion deflection.

Experiments of the ion deflection demonstrate that ions are deflected by the magnetic field, causing a measurable differential current between cathodes. Since the Coriolis force has the same effect on ions as the magnetic field, our experimental conclusions can also be applied to ion deflection by the Coriolis force. Thus, the ion beam gyroscope is feasible and worthy of further exploration.

Considering the variety of constraints, a device with the following variables is chosen for the ion beam gyroscope sensitivity discussion with an optimal performance:

- The discharge distance is 10 mm (0.4 inch) to maintain a small size and reasonable sensitivity.
- The discharge current is 32 μA to achieve a higher signal-to-noise ratio.
- The argon pressure is 2 torr since a high percentage of argon and a small breakdown voltage can be attained.
- The pin-plate structure device is favored with a higher sensitivity than the pin-pin structure.

This discharge device provides a sensitivity of 0.018 μA/mT according to Figure 4.20(b). Equation (3.11) illustrates the conversion between the magnetic acceleration and the Coriolis acceleration in vacuum. However, the pressure level for our experiments are from 1 to 10 torr, where the collisions between ions and neutral particles should be taken into consideration. Since collisions modulate the drift velocity of ions in the x axis, the acceleration produced by the magnetic field is modified as

$$a_p(l) = qv_{(p,x)}B$$

where $v_{p,x}$ is the drift velocity along the x axis which is modulated by gas pressures. Similarly, the imaginary deflection experiments by Coriolis effect would be operating at the

same pressure condition as the magnetic field deflection experiments. The modulated Coriolis acceleration can be described by

$$a_l(c) = -2\Omega \times v_{(p,x)}$$

Therefore, to provide the same magnitude of the accelerating rate produced by the magnetic field, the rotating speed of a platform is

$$a_c = -a_l = -\frac{qB}{2m}$$

Accordingly, we can examine the rotating speed to provide the same acceleration rate as 1 mT magnetic field on the ion.

$$\Omega = -\frac{qB}{2m} = -\frac{1.6 \times 10^{-19} \times 10^{-3}}{2 \times 6.63 \times 10^{-26}} = -1200\ rad/s = -11500\ rpm \tag{4.8}$$

With a rotating speed of 11500 rpm, the ion beam gyroscope produces a differential current of 0.018 μA. The earth's magnetic field (0.05 mT) introduces a 0.0009 μA differential current, which limits the gyroscope resolution. This issue can be addressed by using a proper magnetic shielding layer.

4.3.2 Signal Oscillation

As shown in Figure 4.21 (a), a single ion with a charge $q > 0$ is placed close to a conducting sphere with a radius of a at a potential value $V > 0$. The force between the ion and the sphere is described by Coulomb's Law [55]

$$F = qa[\frac{V}{r^3} - \frac{q}{4\pi\epsilon_0(r^2 - a^2)^2}]\vec{r}, \tag{4.9}$$

where r is the distance between the ion and the center of the conducting sphere, ϵ_0 is the vacuum permittivity constant, and $\vec{r}$ is the position vector of the ion.

When the ion goes towards the surface of the sphere conductor, the Coulomb force becomes positive, and it becomes negative when the ion goes against the conductor. The boundary layer distinguishing two regions is $r = a + R$. A thin layer of negatively charged particles is formed on the sphere surface induced by the single ion. This thin layer has an attractive force to single ion. On the other hand, the net charge of the sphere is always positive resulting in a repulsive force to the ion. When $r > a + R$ (the ion is located in Region A), the attractive force is greater than the repulsive force, and ion moves towards the sphere conductor. In contrast, when the ion enters Region B, (where $r_0 < a + R$), the repulsive force dominates and the ion moves away from the conductor.

This mechanism explains the appearance of the output signal oscillations in the corona discharge [32, 56]. In the corona discharge experiment, there is also an external electric

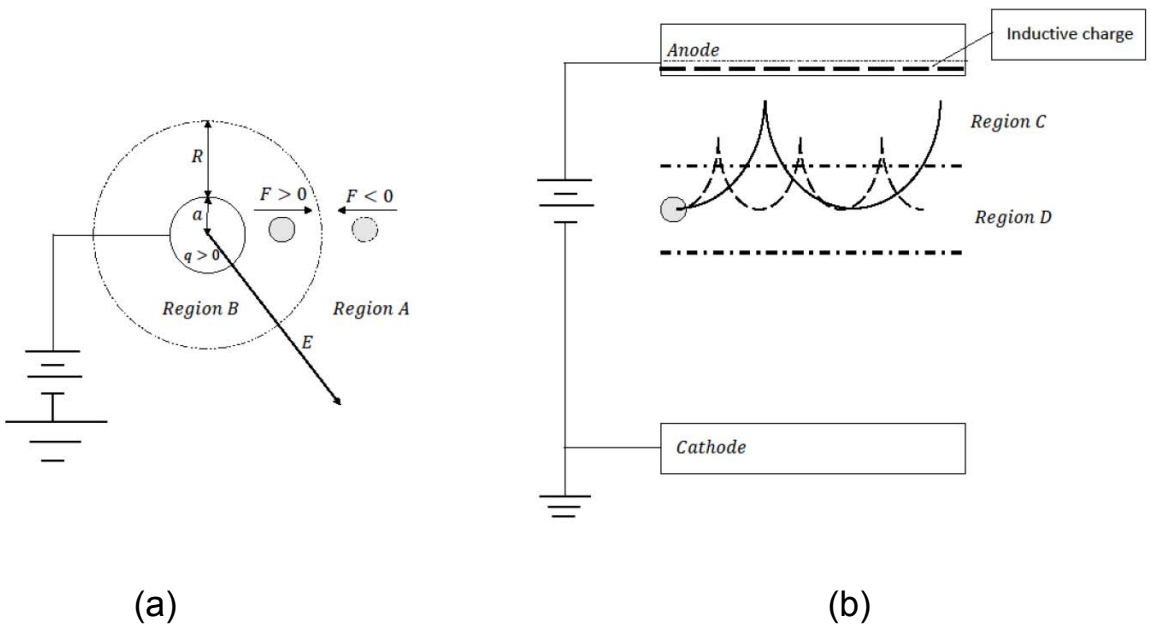

Figure 4.21: Mechanism of corona discharge oscillations: (a) the conductor-to-ion configuration, and (b) the discharge tube with an electric field

field between electrodes, playing a role in modifying the ion path. This makes the corona oscillation slightly different from the conductor-ion configuration.

Figure 4.21 (b) illustrates the scenario of the positive DC corona discharge. Gas discharges produce a large number of ions, which polarize the anode known as the electrostatic effect. The lower side of the anode forms a thin layer of negative inductive charge, which produces an attractive force between the anode and each ion. Moreover, the net charge of the anode is positive, which provides a repulsive force between the anode and ions. When an ion is located in Region C, the repulsive force is larger than the attractive force, so the Coulomb resultant force between the anode and ions is negative. With the effect of the repulsive force, the ion is pushed towards the cathode and leaves Region C to move to Region D. Upon arriving in Region D, the attractive force dominates, and Coulomb resultant force becomes positive. Consequently, the Coulomb force pulls the ion backwards to Region C. Once the ion moves back to Region C, it would be pushed to Region D in the other way around. The pushing and pulling processes cause the ion to move back and forth between Region C and Region D, which causes oscillations. In Figure 4.21 (b), the solid line describes the path of ions without considering the external electric field.

On the other hand, a constant electric field exists in the discharge tube, which also moves the ion. This external electric force drifts ions towards the cathodes, which can be taken as an additional repulsive force between the anode and the ion. Therefore, ions are pushed further in Region C than the case without the electric field. If the ion is located in Region

D, though the attractive force dominates, the Coulomb resultant force becomes smaller considering the repulsion produced by the electric field. In Figure 4.21 (b), the dotted line describes the ion paths with the drift field. The movement of the ion is asymmetrical in those two regions. Besides Coulomb's interaction between the anode and ions, the space charge effect also contributes to the corona oscillation since the ions can also polarize the plasma region.

Theoretically, variables that affecting the spatial distribution of ions, like the discharge current and gas pressures, can also influence the oscillation patterns. To verify our speculation, experiments were conducted on a pin-plate device with a discharge distance of 14.2 mm. Results demonstrate that the oscillation pattern changes with the gas pressure, the discharge voltage, and the discharge current.

The oscillation frequency will be affected by multiple mechanisms. Both the Coulomb force and the space charge effect contribute to ion oscillations. For example, Figure 4.22 (b) has only one oscillation pattern, which is thought to be the impact of one oscillation mechanism, and the other oscillation pattern is weak enough to be neglected. In contrast, Figure 4.22 (d) has multiple oscillation patterns, which is thought to be the combination of both the anode-ion effect and the space charge effect. Since the add-on oscillation is a common mode signal for the dual outputs, it can be canceled by taking the differential current between the two cathodes. Therefore, the output signal with corona oscillations will not affect the sensitivity of ion deflections. Nevertheless, it can saturate the signal processing module unexpectedly if the oscillation amplitude is too large, which in turn affects the observation of the output signals.

4.3.3 Noise Analysis

Instrumental Noise

There are three major noise sources in the experiments from the instrumental side: the high-voltage circuit, the current-voltage conversion circuit and the DAQ system. Experiments demonstrate the noise from DAQ system dominates, and it introduces a current noise of 0.0014 μA while the total instrumental noise is approximately 0.0018 μA. In contrast, the pin-plate discharge device with $d = 10\ mm$ has a differential current of 0.018 μA at a magnetic field of 1 mT. The differential current is 10 times the instrumental noise. Therefore, the experimental setup is adequate for this exploring stage of the ion beam gyroscope.

Signal-to-noise Ratio

Besides the instrumental noise, the discharge current also produces intrinsic noise and is coupled with interference from the environment, which prevents us from improving the

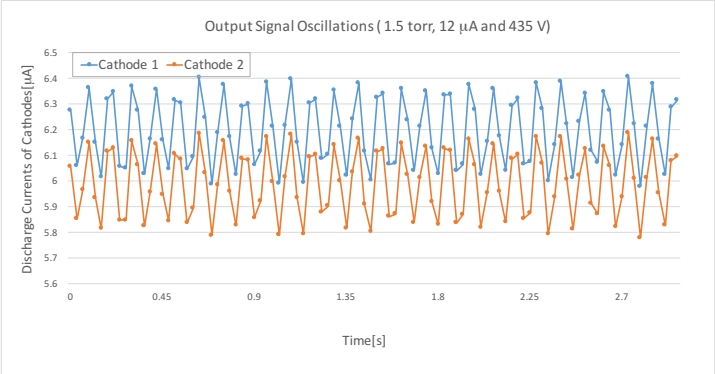

(a) 1.5 torr, 435 V

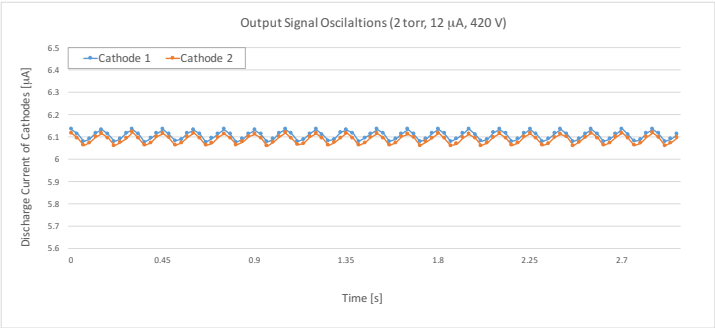

(b) 2 torr, 420 V

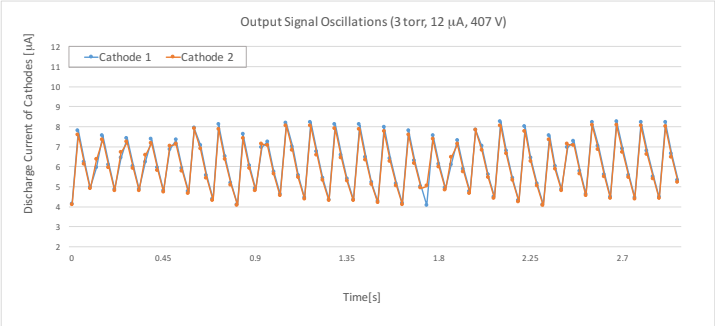

(c) 3 torr, 407 V

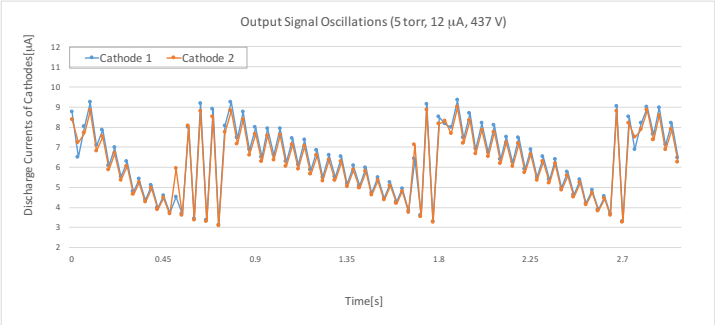

(d) 5 torr, 435 V

Figure 4.22: Discharge current oscillations at 12 μA with Device A

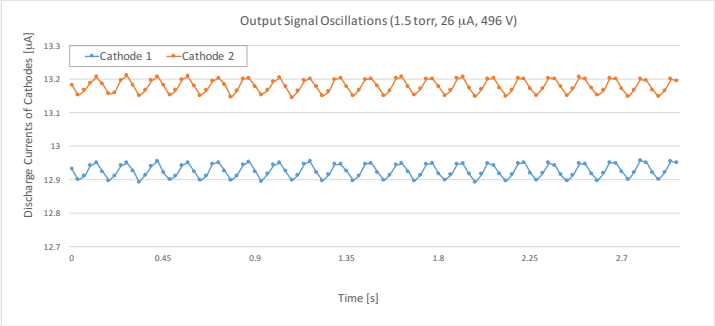

(a) 1.5 torr, 496 V

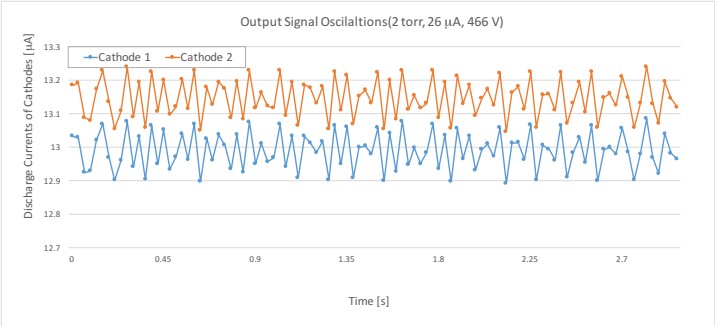

(b) 2 torr, 466 V

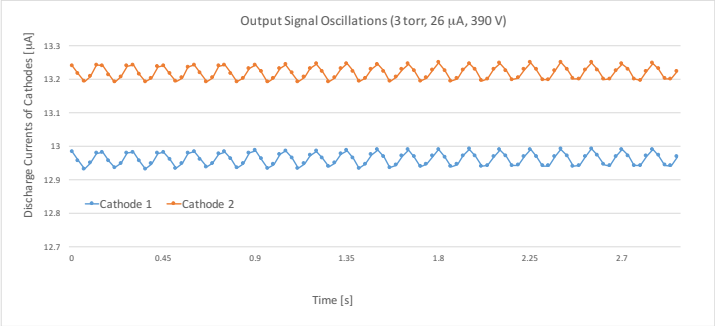

(c) 3 torr, 390 V

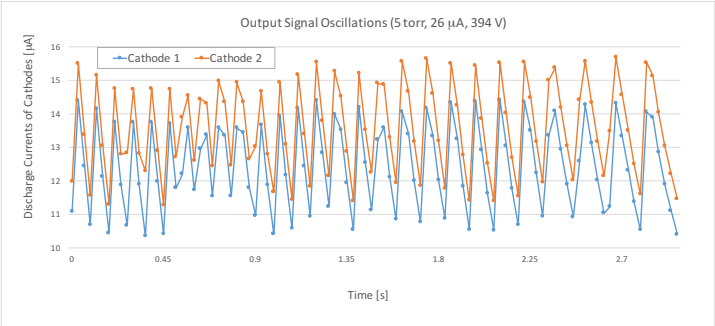

(d) 5 torr, 394 V

Figure 4.23: Discharge current oscillations at 26 μA with Device A

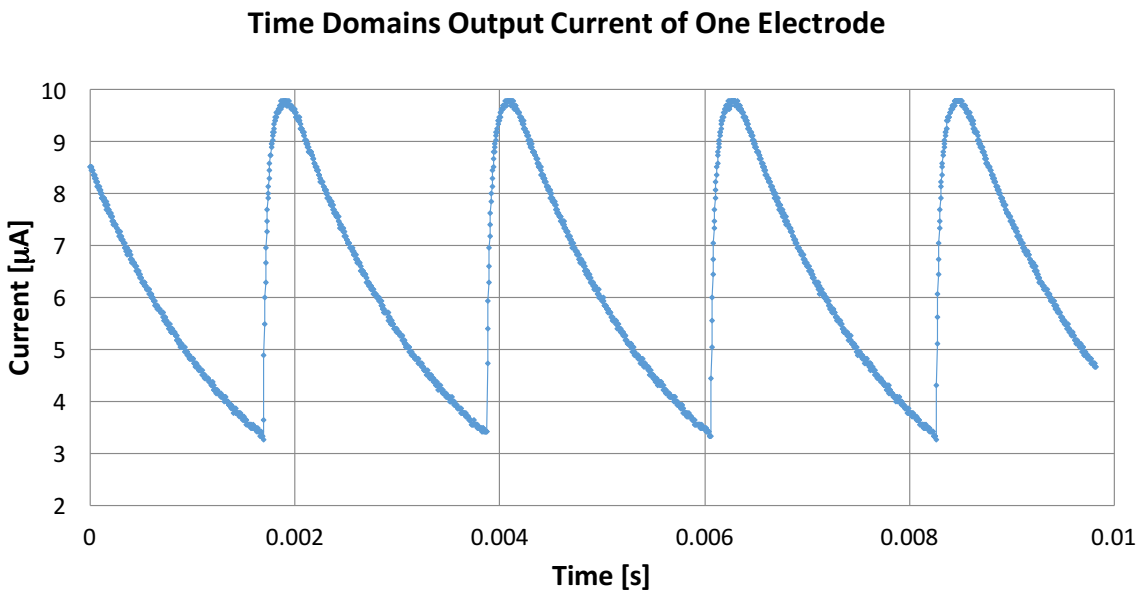

Figure 4.24: Time series current signal at 12 μA with a corona oscillation period of 0.00242 s

resolution of the ion beam gyroscope. We supplied the device with a discharge current of 12 μA at 2 torr. The time series output signal of Cathode 1 is plotted in Figure 4.24.

According to the plot, the corona oscillation is significant and the estimated oscillation period of it is 0.00242 s. Thus, we can deduce that there will be a great signal amplitude at a frequency of approximately 400 Hz, where is the fundamental wave of the oscillation. Fast Fourier transformations (FFT) were done to determine the signal-to-noise ratio (SNR) of Cathode 1. 1024 data points were recorded with a sampling frequency of 4 Hz. Consequently, the resolution of this FFT is

$$R = \frac{F_s}{N} = \frac{4}{1024} = 4 \times 10^{-3}\ Hz/point \tag{4.10}$$

The plotting of the power intensity with frequency is shown in Figure 4.25. The DC offset signal of Cathode 1 has a power intensity of -30.57 dB. Interference coupled from the AC power line at 60 Hz has an intensity of -44.97 dB. Corresponding harmonic wave appears at 180 Hz. The 60 Hz interference is a common mode signal, which can be canceled out by taking the differential signals. Alternatively, a low-pass filter with a cut-off frequency of 10 Hz can be used at the output stage to eliminate the effect of the 60 Hz interference and other high frequency intrinsic noises. Hence, the SNR of the current on Cathode 1 is not greater than,

$$SNR_{dB} = \frac{P_{signal}}{P_{noise}} = -30.57 - (-69.77) = 39.2\ dB$$

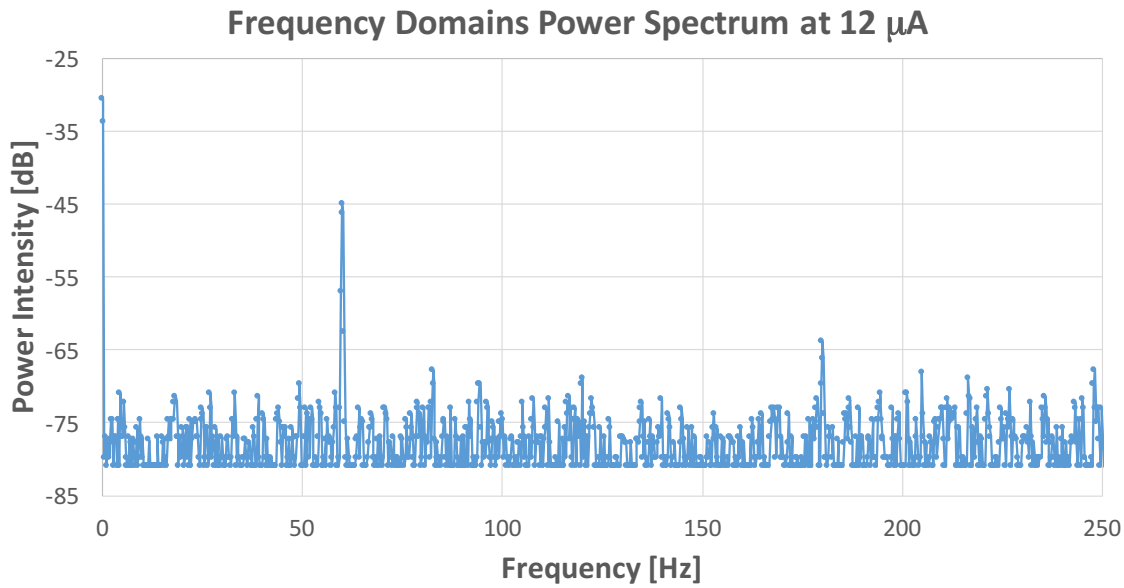

Figure 4.25: Frequency domains power spectrum at 12 μA

Discharge Current (μA)	Signal Intensity (dB)	Noise Intensity (dB)	SNR_{dB}
12	-30.57	-69.77	39.2
26	-17.37	-69.37	50
32	-15.17	-70.57	55.4

Table 4.1: Comparison of SNR values at various discharge currents

Empirically, increasing the discharge current will result in a larger SNR. Therefore, the comparison experiments were conducted with discharge currents of 26 μA and 32 μA. Their FFT plots are shown in Figure 4.26. SNR values of relative discharge current have been calculated and are listed in Table 4.1.

Hence, we can conclude that increasing the discharge current allows us to obtain a higher SNR. Taking the discharge current of 32 μA as an example, the SNR_{dB} value is 55.4dB. For an ideal discharge device, two cathodes are identical in gas discharges, so the discharge current will be allocated equally to two cathodes. Thus, the current of Cathode 1 is 16 μA.

$$SNR = 10^{SNR_{dB}/10} = 10^{5.54}$$

Therefore, the amplitude of the current noise of Cathode 1 is,

$$A_{noise} = \sqrt{\frac{A_{signal}^2}{SNR}} = 0.027\ \mu A$$

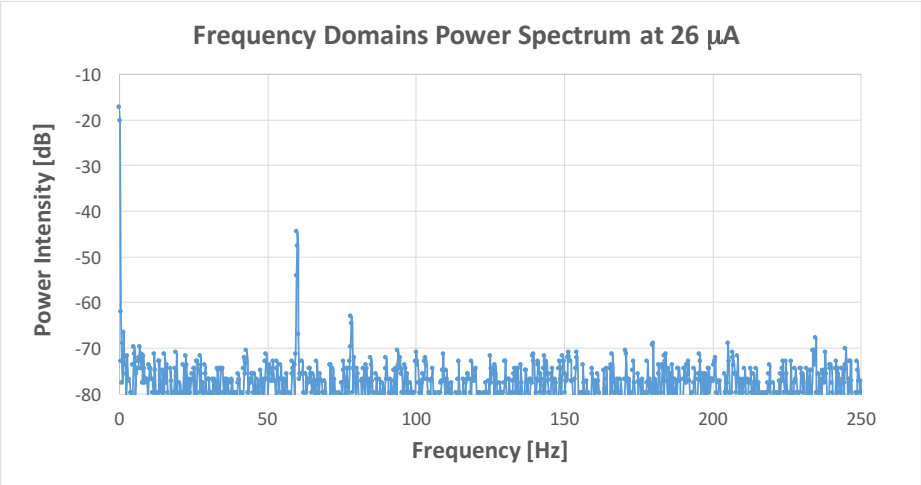

(a) With a discharge current of 26 μA

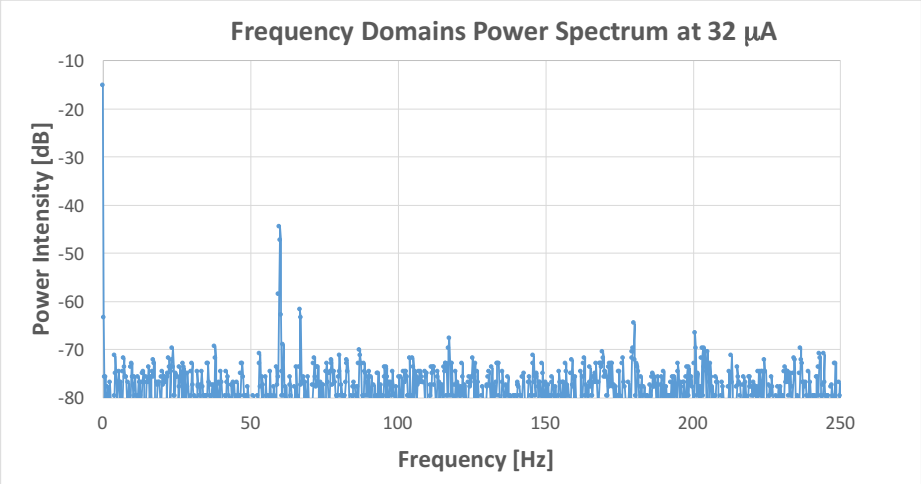

(b) With a discharge current of 32 μA

Figure 4.26: Frequency domains power spectrum with various currents

To summarize, the interference of the earth magnetic field is 0.0009 μA, instrumental noise is 0.0018 μA, and the intrinsic current noise is approximately 0.027 μA for Cathode 1 with the total current of 16 μA.

Chapter 5

Conclusion And Future Work

5.1 Conclusion

In the thesis, a magnetic field is used to simulate the Coriolis acceleration to explore the feasibility of the ion beam gyroscope in the early stage. Ions are generated from gas discharge in a low vacuum chamber with an electric field from 1.5×10^4 to 3×10^5 V/m. A theoretical model of the ion deflection is proposed to study the relevant variables and their influence on the performance of the sensor. Our model shows that the differential current is proportional to the displacement along the y axis, and it increases linearly with the external magnetic field. This model also demonstrates the pressure, the discharge voltage, and the discharge distance have an impact on the ion beam displacement.

Extensive experiments were carried out to verify the theoretical model. The results of those experiments illustrate that ion deflection can be detected by taking the differential signal of the dual electrodes. It also shows that both the differential current and the percentage of deflected ions are proportional to the displacement y. Through the experiments, we also find two limitations of our model. First, according to our observation, the discharge current, the pressure and the discharge distance have non-negligible influences on the discharge voltage. But in our theoretical model, we assume the discharge voltage is an independent variable. Due to the assumption, our theoretical model cannot perfectly match with the experimental results. But it can correctly predict the increase or decrease of the ion deflection with respect to each variable, which is valuable in improving the sensitivity of the gyroscope. Second, this model does not include all variables. For example, later experiments show that a larger cathode area will result in a larger percentage of ion deflection. A larger discharge current will lead to a smaller percentage of ion deflection. So the experimental results are a complement to the theoretical model.

Experimental data show that the sensitivity is proportional to the discharge distance. As for the discharge current, larger discharge current diverges the ion beam, which decreases the sensitivity of deflection experiments. The operating pressure has a weak negative correlation

with the sensitivity. Meanwhile, corona oscillations are observed, which sets obstacles for the output signal measurement. A discharge device with a sensitivity of 0.018 μA/mT has been chosen as the optimal device for the ion beam gyroscope exploration. The corresponding sensitivity of the ion beam gyroscope can be calculated:

$$Sen = \frac{0.018}{11500} = 1.6 \times 10^{-6}\ \mu A/rpm$$

There are several noise sources that affect the resolution of our gyroscope, and the intrinsic noise of the discharge current dominates. Besides that, the earth magnetic field produces an interference of $\pm$ 0.0009 μA. High frequency noise and interference from the AC power line can be avoided using a low pass filter.

5.2 Future Work

The continuous work can be divided into two parts: (1) Replace the magnetic field with a rotating platform, which has an adjustable speed; (2) Improve the performance of ion beam gyroscopes.

When using a rotating platform, the magnetic force produced by the magnetic field is replaced by a Coriolis force. A platform with an adjustable rotating speed can provide various Coriolis acceleration rates, which allows us to directly find out the sensitivity of the ion beam gyroscope.

The current device gives us an ion beam gyroscope with a sensitivity of $1.6\times10^{-6}\ \mu A/rpm$, which is not sensitive enough to be commercialized. A two-stage ion beam gyroscope is proposed that consists of a cathode grid and a pair of grounded cathodes as shown in Figure 5.1. The first stage is a pin-pin structure that has a high discharge voltage and a short discharge distance to generate a convergent ion beam. The cathode grid is a very thin wire supplied with a low voltage, which allows the majority of ions generated in the first stage to pass over it. As a result, ions enter the second stage with an initial speed. The drifting field in the second stage is weak causing a small drifting velocity of the ion beam. Hence, ions are able to travel further along the y axis. Consequently, the differential current is thought to have a larger amplitude.

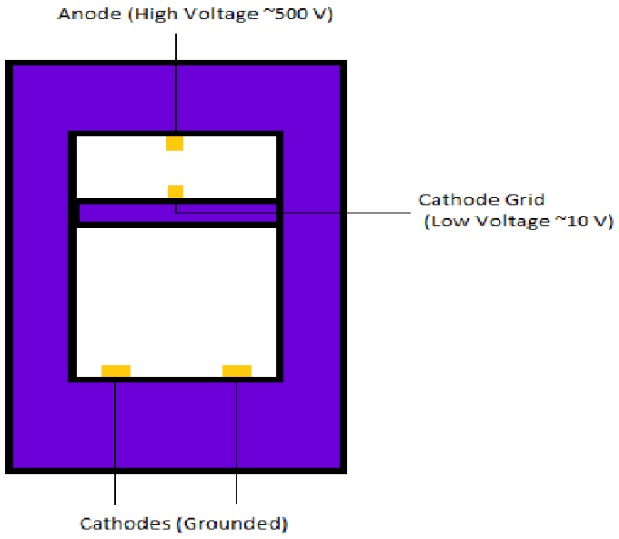

Figure 5.1: The modified discharge device with a grid cathode and grounded cathodes

Bibliography

[1] Aaron Burg, Azeem Meruani, Bob Sandheinrich, and Michael Wickmann. Mems gyroscopes and their applications. *Introduction to Microelectromechanical System, Northwestern University*, 2011.

[2] Christopher Fell and Rebecca Eley. Vibrating structure gyroscopes, October 15 2013. US Patent 8,555,717.

[3] Joseph R Demers, Ka Kha Wong, and Ronald T Logan Jr. Fiber optic gyroscope, June 29 2010. US Patent 7,746,476.

[4] Jamal Bahari, Rui Feng, and Albert M Leung. Robust mems gyroscope based on thermal principles. *Journal of Microelectromechanical Systems*, 23(1):100–116, 2014.

[5] Steven C Frautschi, Richard P Olenick, and Tom M Apostol. *The mechanical universe: Mechanics and heat*. Cambridge University Press, 2007.

[6] Richard P Feynman, Robert B Leighton, and Matthew Sands. *The Feynman Lectures on Physics, Desktop Edition*, volume 1. Basic books, 2013.

[7] V Amoruso and F Lattarulo. Accurate extension of Peek's law to stranded conductors. *International Transactions on Electrical Energy Systems*, 1(1):15–20, 1991.

[8] John M Meek and John Drummond Craggs. Electrical breakdown of gases. 1978.

[9] MMA Salama, H Parekh, and KD Srivastava. Model for switching surge breakdown of a point-to-plane air gap. *Journal of Applied Physics*, 47(10):4426–4429, 1976.

[10] J-S Chang, Phil A Lawless, and Toshiaki Yamamoto. Corona discharge processes. *IEEE Transactions on plasma science*, 19(6):1152–1166, 1991.

[11] MN Shipko, VG Kostishin, MA Stepovich, and VV Korovushkin. Modifying the properties of ferrite materials with a hexagonal structure via treatment in corona discharge plasma. *Journal of Surface Investigation: X-ray, Synchrotron and Neutron Techniques*, 11(1):142–145, 2017.

[12] Jihyeon Lee, Sehwan Park, Soo Gyeong Cho, Eun Mee Goh, Sungman Lee, Sung-Suk Koh, and Jeongkwon Kim. Analysis of explosives using corona discharge ionization combined with ion mobility spectrometry–mass spectrometry. *Talanta*, 120:64–70, 2014.

[13] Dong-Joo Kim and Kyo-Seon Kim. Analysis on plasma chemistry and particle growth in corona discharge process using discrete-sectional method. *IEEE transactions on plasma science*, 31(2):227–235, 2003.

[14] Z Mokhtari, S Hole, and J Lewiner. Smoke triggered corona discharge sensor. *Journal of Electrostatics*, 71(4):769–772, 2013.

[15] Beelee Chua and Ahjeong Son. Sensing absolute air pressure using micro corona discharge. *Sensors and Actuators A: Physical*, 217:49–55, 2014.

[16] M Cerdonio, M Bonaldi, P Falferi, GA Prodi, and S Vitale. A gyromagnetic electron gyroscope. *Japanese Journal of Applied Physics*, 26(S3-2):1669, 1987.

[17] James V Johnston. Electron gyroscope, December 8 1964. US Patent 3,160,018.

[18] Vashwar Tajdidur Rouf, Mo Li, and David A Horsley. Area-efficient three axis mems lorentz force magnetometer. *IEEE Sensors Journal*, 13(11):4474–4481, 2013.

[19] Matthew J Thompson and David A Horsley. Parametrically amplified z-axis lorentz force magnetometer. *Journal of Microelectromechanical Systems*, 20(3):702–710, 2011.

[20] Mo Li, Soner Sonmezoglu, and David A Horsley. Extended bandwidth lorentz force magnetometer based on quadrature frequency modulation. *Journal of Microelectromechanical Systems*, 24(2):333–342, 2015.

[21] Edward Ramsden. *Hall-effect sensors: theory and application*. Newnes, 2011.

[22] Alexander Piel. *Plasma physics: an introduction to laboratory, space, and fusion plasmas*. Springer Science & Business Media, 2010.

[23] John P Dakin and Robert GW Brown. *Handbook of Optoelectronics (two-volume set)*. CRC Press, 2006.

[24] John Kuffel and Peter Kuffel. *High voltage engineering fundamentals*. Newnes, 2000.

[25] John Sealy Townsend. *Electricity in gases*. Clarendon Press, 1915.

[26] Melvin A Harrison and Ronald Geballe. Simultaneous measurement of ionization and attachment coefficients. *Physical Review*, 91(1):1, 1953.

[27] Leonard B Loeb. *Fundamental processes of electrical discharge in gases*. John Wiley & Sons, 1939.

[28] Lawrence E Tannas. *Flat-panel displays and CRTs*. Springer Science & Business Media, 2012.

[29] Alexander Fridman. *Plasma chemistry*. Cambridge University Press, 2008.

[30] KG Emeleus. The Faraday dark space. In *Proceedings of the Royal Irish Academy. Section A: Mathematical and Physical Sciences*, pages 31–36. JSTOR, 1934.

[31] VA Lisovskiy and SD Yakovin. Experimental study of a low-pressure glow discharge in air in large-diameter discharge tubes: I. conditions for the normal regime of a glow discharge. *Plasma Physics Reports*, 26(12):1066–1075, 2000.

[32] M Goldman, A Goldman, and RS Sigmond. The corona discharge, its properties and specific uses. *Pure and Applied Chemistry*, 57(9):1353–1362, 1985.

[33] Frank William Peek. *Dielectric phenomena in high voltage engineering*. McGraw-Hill Book Company, Incorporated, 1920.

[34] JJ Lowke and F D'Alessandro. Onset corona fields and electrical breakdown criteria. *Journal of Physics D: Applied Physics*, 36(21):2673, 2003.

[35] Xianlong Wei, Sheng Wang, Qing Chen, and Lianmao Peng. Breakdown of Richardson's law in electron emission from individual self-joule-heated carbon nanotubes. *Scientific reports*, 4, 2014.

[36] IG Brown, JE Galvin, BF Gavin, and RA MacGill. Metal vapor vacuum arc ion source. *Review of scientific instruments*, 57(6):1069–1084, 1986.

[37] Hertha Ayrton. *The electric arc*. Cambridge University Press, 2012.

[38] Alan D McNaught. *Compendium of chemical terminology*, volume 1669. Blackwell Science Oxford, 1997.

[39] H Ait Said, H Nouri, and Y Zebboudj. Effect of air flow on corona discharge in wire-to-plate electrostatic precipitator. *Journal of Electrostatics*, 73:19–25, 2015.

[40] VGI Deshmukh and TI Cox. Physical characterisation of dry etching plasmas used in semiconductor fabrication. *Plasma Physics and Controlled Fusion*, 30(1):21, 1988.

[41] Z Mokhtari, S Holé, and J Lewiner. Study of an ionic smoke sensor. *Measurement Science and Technology*, 24(5):055006, 2013.

[42] Antonio Castellanos, Antonio Ramos, Antonio Gonzalez, Nicolas G Green, and Hywel Morgan. Electrohydrodynamics and dielectrophoresis in microsystems: scaling laws. *Journal of Physics D: Applied Physics*, 36(20):2584, 2003.

[43] Theodore Soller, Merle Arthur Starr, and George Edward Valley. *Cathode ray tube displays*. Dover Publications, 1948.

[44] John R de Laeter, John Karl Böhlke, P De Bièvre, H Hidaka, HS Peiser, KJR Rosman, and PDP Taylor. Atomic weights of the elements. review 2000 (iupac technical report). *Pure and applied chemistry*, 75(6):683–800, 2003.

[45] Wolfgang Jitschin, Felix Sharipov, Rudolf Lachenmann, and Karl Jousten. *Wutz Handbuch Vakuumtechnik*. Springer-Verlag, 2009.

[46] Gregory H Wannier. Motion of gaseous ions in strong electric fields. *The Bell System Technical Journal*, 32(1):170–254, 1953.

[47] John A Hornbeck. The drift velocities of molecular and atomic ions in helium, neon, and argon. *Physical Review*, 84(4):615, 1951.

[48] Richard P Feynman, Robert B Leighton, Matthew Sands, and R Bruce Lindsay. The feynman lectures on physics, vol. 3: Quantum mechanics, 1966.

[49] Kermit K Murray, Robert K Boyd, Marcos N Eberlin, G John Langley, Liang Li, and Yasuhide Naito. Definitions of terms relating to mass spectrometry (iupac recommendations 2013). *Pure and Applied Chemistry*, 85(7):1515–1609, 2013.

[50] Ekram Husain and RS Nema. Analysis of Paschen curves for air, N2 and SF6 using the Townsend breakdown equation. *IEEE transactions on electrical insulation*, (4):350–353, 1982.

[51] MI Large. A relaxation oscillation maintained by discharge corona. *Nature*, 179:707–708, 1957.

[52] Sung Nae Cho. Physics of self-sustained oscillations in the positive glow corona. *Physics of Plasmas*, 19(7):072113, 2012.

[53] Rajib Mahamud and Tanvir I Farouk. Ion kinetics and self pulsing in dc microplasma discharges at atmospheric and higher pressure. *Journal of Physics D: Applied Physics*, 49(14):145202, 2016.

[54] KTAL Burm. Calculation of the Townsend discharge coefficients and the Paschen curve coefficients. *Contributions to Plasma Physics*, 47(3):177–182, 2007.

[55] Raymond Matthew Fuoss and Filippo Accascina. *Electrolytic conductance*. Interscience Publishers, 1959.

[56] N Sato. Discharge current induced by the motion of charged particles. *Journal of Physics D: Applied Physics*, 13(1):L3, 1980.